Study on Electrode Materials for Lithium-Ion Batteries by Neutron Scattering and X-Ray Diffraction

Doctoral Thesis

by

S. M. Mostafa Al Mamun[1]

Department of Materials Structure Science
School of Mathematical and Physical Science
The Graduate University for Advanced Studies
Hayama, Kanagawa 240-0193, JAPAN

March 2002

[1]On study leave: Assistant Professor, Dept. of Applied Physics & Electronics, Dhaka University, Dhaka-1000, BANGLADESH

Abstract

Disordered carbons play a significant role as anode materials in recent developments of rechargeable Li-ion batteries with attractive features such as long cycle life and higher lithium capacity per mass of carbon. They also present major challenges in determining structure-property relationships, in particular the location, density and properties of the sites at which Li can be reversibly intercalated. Attempts to understand the nanoscopic physics and chemistry of reversible Li uptake in these materials are frustrated by the lack of long-range order. Diffraction, microscopy, NMR, gas adsorption etc. can not fully determine the nanoscopic structure and lithium sites, and a variety of controversial models and explanations for Li sites have been suggested in the literature.

By small angle neutron scattering (SANS) we directly observed nanopores with radius of gyration ~ 7 Å in our disordered hard carbon sample and confirmed that Li reversibly intercalates into the graphene layer spacings and inside the nanopores. These nanopores are ascribed to the origin of higher capacity (LiC_5) of our sample. We also calculated the volume fraction of these nanopores as $\sim 16\%$ in this material, which has a strong correlation with the capacity difference between our sample and pure graphite (LiC_6). ^{7}Li-NMR study by K. Tatsumi at low temperatures showed variation in signal intensity suggesting diffusive behaviour of Li atoms between the sites. But in SANS measurements on fully lithiated hard carbon sample we did not observe any change concerning d-spacing and pore size between room temperature and low temperature data suggesting no net diffusion of Li species from pore site to layer site and vice versa at low temperature.

Effect of jet-milling on Swedish natural graphite (Woxna) was also studied. Woxna shows increased capacity after jet-milling and different cycle performance between crude and jet-milled samples. It was suspected that jet-milling might introduce some pores in the sample but no nanopore structure was observed from SANS measurement. Rather, we observed some changes in the hexagonal (AB) and rhombohedral (ABC) phase content by neutron powder diffraction (NPD) measurements. It was also confirmed by in-situ x-ray diffraction study that jet-milling does not destroy the staging property of Woxna.

Contents

List of Figures

List of Tables

Chapter 1

Introduction

1.1 Objective

Three kinds of carbon have been used as anodes for commercial lithium-ion cells: graphite, soft carbon and hard carbon. Graphite is a three-dimensional ordered crystal that can intercalate up to a maximum of one lithium atom per six carbon atoms (LiC_6) giving a maximum capacity of 372 $mAh{\cdot}g^{-1}$. Soft carbon and hard carbon constructed with two-dimensional ordered graphene sheets which are randomly stacked [1] and form 'turbostratic' structure. Many soft carbons show a maximum reversible capacity of about 300 $mAh{\cdot}g^{-1}$ when heat treated around 1200 °C [2]. Lithium can be doped to some hard carbons up to over one lithium atom per six carbon atoms and some of them offer over 500 $mAh{\cdot}g^{-1}$ of reversible capacity with a small irreversible capacity of about 60 $mAh{\cdot}g^{-1}$ [3].

Disordered carbons play a significant role as anode materials in recent developments of rechargeable Li-ion batteries with attractive features such as long cycle life and higher lithium capacity per mass of carbon. They also present major challenges in determining structure-property relationships, in particular the location, density and properties of the sites at which Li can be reversibly intercalated. Attempts to understand the nanoscopic physics and chemistry of reversible Li uptake in these materials are frustrated by the lack of long-range order. The usual structure probes (diffraction, microscopy, NMR, gas adsorption etc.) give only limited information concerning the location of intercalated Li in disordered carbons. In 1997, Y. Nishi, [4], without any direct evidence, proposed nanopore structure model (Fig.1.1) in hard carbons to justify the high capacity. To rationalize the high 'extra' lithium capacity of hard carbons, still a variety of controversial models and explanations for Li sites have been suggested in the literature:

- R. Yazami [5] proposed the formation of lithium multilayers on the graphene sheets.
- E. Peled [6] believe that the extra charge is attributed to the accommodation of lithium in "zigzag" and "arm-chair" faces between two adjacent crystallites and in the vicinity of the defects and impurities.

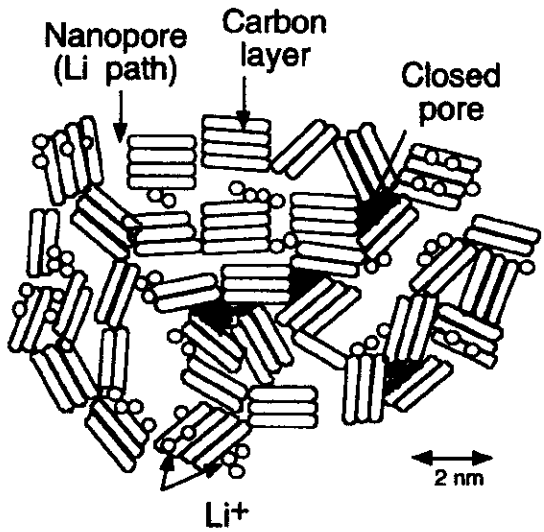

Figure 1.1: Lithium trapping sites in hard carbon;
Model of Y. Nishi, 1997.

- K. Sato [7] suggested that lithium occupies nearest neighbour sites in intercalated carbons; and so many other opinions.

Thus it has been impossible so far by traditional techniques to establish the general structure-property relationships, which is necessary to optimize the battery performance of these materials.

Small angle neutron scattering (SANS) technique represents a novel and alternative with a number of advantages. SANS is sensitive to both closed and open pores and in many cases offers a more complete picture of porosity. It can also be applied to wet samples. SANS is more efficient and accurate than SAXS because scattering contrast between carbon matrix (with or without lithiated) and pore is more for neutrons resulting in higher intensity [8]. In addition, the wide Q range (0.002—2.0 $Å^{-1}$) that has been achieved in our instrument (SWAN) [9], enabled us to analyze data from the nanopore down to the d-spacing range of graphene layers.

As a candidate for hard carbon we studied carbon fiber prepared from an isotropic petroleum pitch (nominal diameter of 10 μm, HTT 1200 °C, FIP, Petoca Ltd.), a precursor of disordered non-graphitizable carbon. This material is found promising because in addition to high capacity it also provides a significant performance in the potential range from 0 to 0.1 V (vs. Li/Li^+) (Fig.3.26) [10]. The capacity below 0.1 V looks like a plateau during charge and discharge and is very attractive for anodes of high energy-density batteries. ^{7}Li-NMR study by K. Tatsumi [11] on this sample only revealed two kinds of Li species at fully lithiated state, but there was no direct indication about the nanoscopic structure and Li sites. SANS measurements provided us all these necessary information.

In addition, Swedish natural graphite (Woxna) and Meso carbon micro beads (MCMB) were also studied as candidates for graphite and soft carbon, respectively.

Woxna shows increased capacity after jet-milling and different cycle performance between crude and jet-milled samples. It was suspected that jet-milling might introduce some pores in the sample but no nanopore structure was observed in SANS measurement. To justify the effect of jet-milling neutron powder diffraction (NPD) experiment was carried out. In parallel in-situ x-ray diffraction study was performed to study the effect of jet-milling on staging property of Woxna.

The purpose of this study is to explore the influence of the structure on the lithium intercalation capacity and electrochemical behaviour of each functional carbon anode material and thus to establish a scientific basis for optimizing their performance in real batteries.

1.2 Li-Ion Battery

1.2.1 Background

In the past few years, there has been a trend toward the proliferation of personal portable electronic devices. One of the key technology developments required to make this transition to cordless operations possible is the availability of small, lightweight, high energy density rechargeable batteries. To meet this demand, a new type of rechargeable battery system, lithium-ion (Li-ion) batteries, has been developed in the last decade. Li-ion batteries offer the advantage of the light weight of lithium without generating volatile lithium metal. This is accomplished by the use of a carbon-based material as the negative electrode for doping and undoping lithium ions.

In comparison to conventional rechargeable battery systems, nickel-cadmium (Ni-Cd) and nickel-metal hydride (Ni-MH) batteries, the lithium ion battery systems have been extensively applied in many applications including portable computers, cellular phones, camcorders, minidisk players, and other portable devices. The total worldwide production of Li-ion batteries in 1996 was 118 million cells [12]. The first Carbon/$LiCoO_2$ Li-ion battery was developed by Sony in 1991. Since then, more than 90% of Li-ion batteries have been produced by Japanese companies such as Sony, Sanyo, Panasonic, AT, and Moli.

Besides being a very high energy density rechargeable system, the Li-ion battery system has the following additional advantages: high voltage per cell, compact size, light weight, rapid recharge capability, environmentally friendly, and safety. These batteries can be made in smaller and lighter sizes than Ni-Cd and Ni-MH batteries. A 30% reduction of battery size and weight is achieved when Li-ion rechargeable batteries are used instead of Ni-MH batteries in PC applications. This reduction is a significant product advantage in the highly competitive portable computer marketplace, and therefore many manufacturers are shifting from Ni-MH to Li-ion batteries. According to the market prediction, the Li-ion battery system will continue to play a crucial role in future in the electronics industry, especially in two of the fastest growing portable device markets: portable computers and cellular telephones.

1.2.2 Chemistry of the Lithium-Ion Cell

Li-ion cells evolved from earlier lithium metal battery technology. The attractions of rechargeable lithium metal batteries have been well known for some time, but they were considered too hazardous for use in consumer products because of the highly reactive lithium metal electrodes whose handling and transportation required special precautions. Primary lithium metal batteries were first used in the 1970's and became widely used in both commercial and military applications. In 1980's rechargeable lithium metal batteries were commercialized. However, they were forced out of the market due to safety issues. The safety problem was related to the reactive, high surface area electroplated lithium metal formation and dendrite growth causing short circuit during the charging process. Early lithium rechargeable systems had been used for more than a decade in military applications. In these applications the advantage of the high energy density of the rechargeable battery was sufficient to justify the stringent precautions required for the safe use of lithium-metal based batteries.

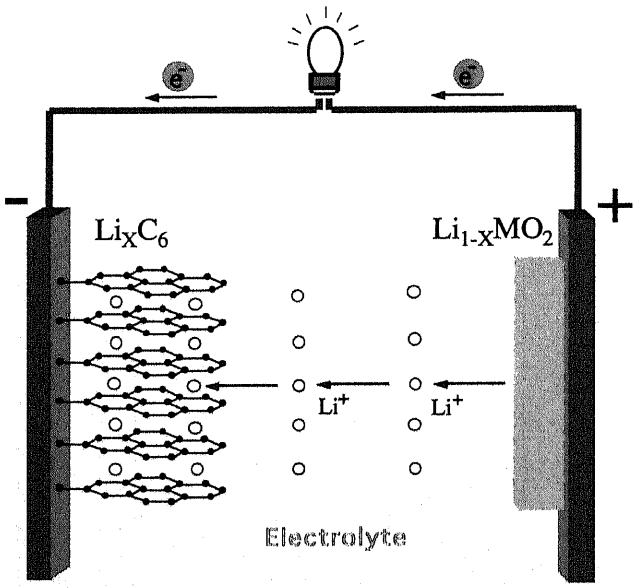

Figure 1.2: Schematic diagram of the Li-Ion secondary battery.

The basic concept for developing the Li-ion battery is to keep lithium in the ionic state thus taking advantage of its electrochemical benefits for rechargeable batteries while eliminating the safety issues associated with metallic lithium. Improvements in safety have been achieved by utilizing lithium intercalation at the anode instead of the early process which was electroplating with lithium metal. The move to a dual intercalation system, sometimes referred to as "rocking chair" technology, in which lithium ions move back and forth during charging and discharging states, resulted in the development of the first commercial Li-ion products (Fig.1.2). Both positive and negative electrodes in the Li-ion cell absorb (interca-

late) and desorb (deintercalate) lithium ions into the active material during charge and discharge.

For most Li-ion systems, carbon is the active material for the negative electrode and Li_xCoO_2 for the positive electrode. The basic chemical reaction governing the Li-ion cell is :

$LiCoO_2 + C = Li_{(1-x)}CoO_2 + Li_xC$

During charge, the reaction proceeds from left to right. On discharge, the reaction reverses and proceeds from right to left.

1.3 Review on carbon materials

There are several commercially available carbon types including natural and synthetic graphites, carbon blacks, active carbons, carbon fibers, cokes, and a wide variety of other materials prepared by the pyrolysis of organic precursors in inert gas. All of these materials reversibly react with lithium to some extent and can be used as the negative electrode (anode) in lithium-ion batteries. To maximize the stored energy per unit mass in these batteries, it is crucial to determine which types of carbon react reversibly with largest amount of lithium per unit mass of carbon.

Carbon materials can be classified in many different ways, disordered versus graphitic, hard versus soft, hydrogen versus non-hydrogen containing, and there are no doubt many other classifications as well. All these carbons are prepared from the pyrolysis of organic precursors. During the early stages of pyrolysis in inert gas (below 600 °C), organic compounds decompose and emit gases that contain carbon, such as CO and CH_4 [13]. The remaining C atoms condense into planar aromatic structures (called graphene sheets) that are terminated predominantly with H atoms at their edges. If the decomposing precursor forms a semifluid state, then these planar sheets can align in a more or less parallel fashion that leads ultimately to easy graphitization upon heating to very high temperatures. Such precursors yield "soft" or graphitizable carbons. However, if the organic precursors is sufficiently cross-linked , then a fluid state is not realized during decomposition and the planar aromatic structures can not align. These materials are difficult to graphitize at any heat treatment temperature and thus are called "hard" or non-graphitizable carbons. During heating in the temperature range from 600 to ~1000 °C, hydrogen is eliminated [13] and the size of the planar graphene sheets grow to ~20 to ~30 Å. In soft carbons, there are regions where 3 to 10 of these sheets are stacked in a more or less parallel fashion, separated by small regions of "unorganized carbon" that may consist of buckled single layers or tetrahedrally bonded carbon [14]. The layers are stacked with random rotations or translations between them, a condition known as turbostratic disorder [15]. In some hard carbons, the graphene sheets do not stack in a parallel way and are in a "house of cards" arrangement. Such carbons inherently have appreciable nanoporosity, with pores on the order of the size of the graphene sheets.

During further heating of soft carbons above 1000 °C, the lateral dimensions

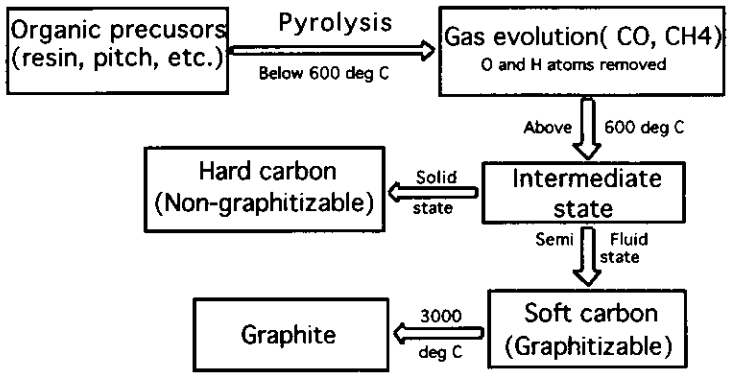

Figure 1.3: Production mechanism of carbon materials.

of the graphene sheets grow to ~150 Å; by 2000 °C, the layers become parallel (with 50 to 100 layers per stack) but turbostratic misalignment is not relieved, apparently because of some "pinning" that prevents the rotation of layers into the normal stacking found in graphite. Only above 2000 °C enough thermal energy is present to overcome this pinning and for the layers to rotate into the registered graphite stacking arrangement. The probability P of finding adjacent graphene sheets on turbostratic misalignment decreases from ~1 at 2000 °C to near 0 for soft carbons heated to ~3000 °C. When all hard carbons are heated above ~1000 °C, the size of the graphite sheets grows and the sheets swing into more or less parallel positions, eliminates the nanoporosity. However, large numbers of parallel layers never form at any heat treatment temperature and turbostratic misalignment is never relieved.

Commercially available carbon materials are classified into three regions. Region 1 contains carbons prepared by heating so-called soft carbon precursors to temperatures above ~2000 °C where well-graphitized materials result. In these materials, the probability P for turbostratic misalignment between adjacent layers decreases with heating temperature. Region 2 contains both soft and hard carbon precursors that contain substantial hydrogen. As the temperature of the samples is increased, the hydrogen content decreases. Region 3 contains hard carbon materials that are made up predominantly of single carbon sheets that contain appreciable nanoporosity and are stacked more or less like a house of cards.

Fig.1.4 shows the voltage-capacity relations for lithium-carbon electrochemical cells made from representative materials from each of the three regions. The synthetic graphite sample gives a reversible capacity of ~355 mAh/g. Petroleum pitch heated to 550 °C to give $H_{0.4}C$ [16] gives a reversible capacity of near 900 mAh/g, one of the largest capacities of any material in region 2. All materials in region 2 are anomalous because their voltage profiles show appreciable hysteresis (lithium inserted near 0.0 V is removed near 1 V). Resole resin heated to 1000 °C has a composition of $H_{0.4}C$ and gives a reversible capacity of ~560 mAh/g, one of the largest capacities known for materials in region 3. The voltage profiles for each

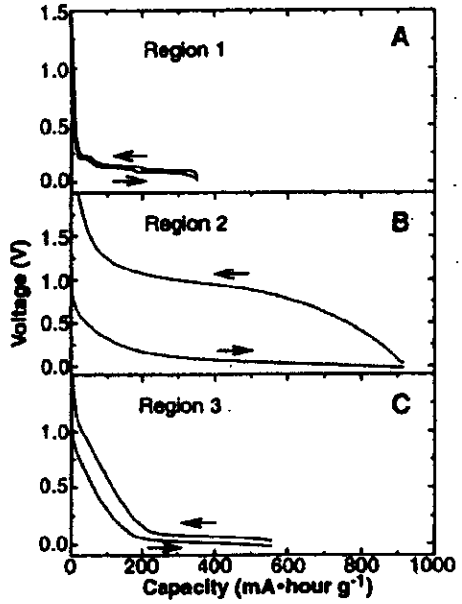

Figure 1.4: Plots of voltage vs. reversible capacity for the second charge-discharge cycle of representative carbon samples. (**A**) Synthetic graphite; (**B**) petroleum pitch; (**C**) resole resin heated to 1000 °C. Arrows designate the directions; the curves are traversed Li is added to (to the right) or removed from (to the left) the carbon samples.

J. R. Dahn [17].

of the materials in Fig.1.4 are markedly different, which suggests that different reaction mechanisms are important in each of the three regions.

1.4 Development of the Carbon Anode

1.4.1 Introduction

Li can be reversibly inserted into graphite to form LiC_6 (Fig.1.5). Carbon anodes became a break through in realizing the lithium "rocking chair" battery and has solved the safety problem of lithium metal anode [18]. The system was first commercialized in 1991 and gave rise to today's development of lithium rechargeable batteries. The choice of carbon anode also matches the current trend toward high performance cathodes, such as $LiCoO_2$, $LiNiO_2$ and $LiMnO_4$.

From the viewpoint of materials science as well as battery applications, carbons attracted much interest because of their diversive characteristics. The diversivity can be attributed to the variety of structures, and it is the structure which plays the most important role in electrochemical performance. The preparation history influences the construction of each carbon structure, and the starting materials also strongly control the structure of the final product. Materials prepared from the solid phase such as organic polymers and resins are highly disordered hard car-

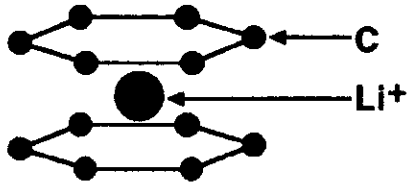

Figure 1.5: The structure of LiC_6.

bons; examples include glassy carbons and some kinds of carbon fibers. Materials synthesized from liquid phase such as petroleum pitch can be highly oriented like petroleum cokes and artificial graphites. A third group comprises products from gas phase, *e.g.*, vapour grown carbon fibers and pyrolytic carbons.

1.4.2 Carbonaceous Host Materials

Most carbons capable of lithium intercalation can roughly be separated into graphitic carbons and non-graphitic (disordered) carbons.

Graphitic carbons are carbonaceous materials having a layered structure but with a number of structural defects. From a strictly crystallographic point of view, the term "graphite" is only applicable to carbon materials having a layered lattice structure with a perfect stacking order of graphene layers, either the more prevalent AB (hexagonal graphite) or the less common ABC (rhombohedral graphite) as shown in Fig.1.6. Due to the small energy required for the transformation of an AB to ABC-stacking (and *vice versa*), perfectly stacked graphite crystals are practically not available. Therefore, the term "graphite" is commonly used regardless of the stacking order.

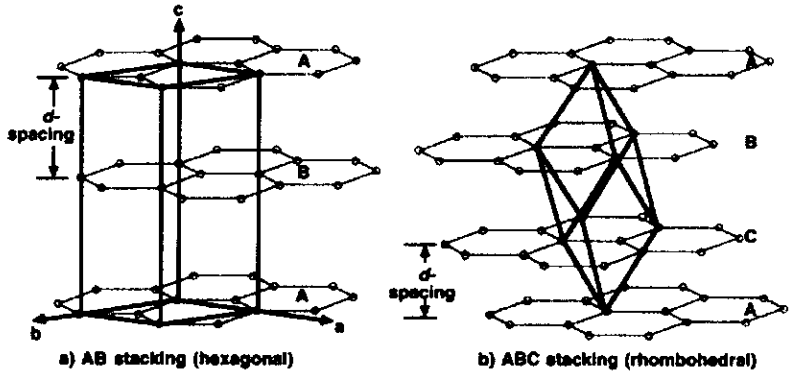

Figure 1.6: Graphite Crystal Structure; thick line a unit cell; (a) the AB stacking (hexagonal cell) and (b) the ABC stacking (rhombohedral cell).

As most materials deviate more or less from the graphite structure, even materials which consists of aggregates of graphite crystallites are named graphites, *e.g.*, the terms natural graphite, artificial or synthetic graphite and pyrolytic graphite

are commonly used, although the materials are polycrystalline [19]. The crystallites may vary considerably in size. In some carbons, the aggregates are large and relatively free of defects, *e.g.*, in highly oriented pyrolytic graphite (HOPG). In addition to graphitic crystallites, some carbons may also include crystallites which contain carbon layers or packages of stacked carbon layers characterized by significant misfits and misorientation angles of the stacked segments to each other called turbostratic disorder [15], leading to higher average layer plane spacing [19, 14].

When turbostratically disordered structure becomes more distinct and dominates among the crystallites, the carbonaceous material is no longer graphitic and can be considered as non-graphitic carbon. Non-graphitic carbonaceous materials consist of carbon atoms with most of them arranged in a planer hexagonal network but without the crystallographic order in the c-direction of the graphite structure. The structure of those carbons is characterized by amorphous areas embedding and crosslinking more graphitic ones [20]. The respective area number and their size vary, depending on the precursor material and the manufacturing temperature.

Non-graphitic carbons are mostly prepared by pyrolysis of organic polymer or hard carbon precursors at at temperatures below ~1500 °C. Further heating of most non-graphitic (disordered) carbons to temperatures between ~1500 - ~3000 °C allows division into two distinctly different carbon types. Graphitizable carbons develop the graphite structure continuously during the heating process since crosslinking between the carbon layers is weak and the layers therefore mobile enough to form graphite-like crystallites. The ability for graphitization is also dependent on the preordering of the respective material. For example, the graphitization ability is higher (i) if the precursor material comprises highly condensed aromatic hydrocarbons, which can be considered to have a graphene-like structure and (ii) if neighbouring graphene layers or graphite crystallites are suitably oriented to each other. Non-graphitizable carbons exhibit no true development of the graphite structure even at high temperatures (2500-3000 °C) since the carbon layers are immobilized by crosslinking.

The mobility of the carbon structure units, which determines the degree of microstructural ordering of the carbonaceous material, is dependent on the state of aggregation of the intermediate phase of the material during pyrolysis, which can be solid, liquid or gaseous [21]. Therefore, non-graphitizable carbons are usually products of the solid-phase pyrolysis whereas graphitizable carbons are commonly produced by liquid or gas phase pyrolysis. Examples of products of the solid-phase pyrolysis are carbonaceous materials like chars and glassy (vitreous) carbon, which are produced by pyrolysis of crosslinked polymers. Because of the small crystal size and high structural disorder of the polymers, the ability of these carbons to graphitize is low. Pyrolysis of thermally stabilized polyacrylonitrile or pitch, which are the precursors for carbon fibers, yields also solid intermediate phases, but stretching of the fibrous material during the manufacturing process produces an ordered microstructure [21]. The synthesis of petroleum coke, which is the most important raw material for the manufacture of carbons and graphite, is an example of liquid-phase pyrolysis. Petroleum coke is produced by the pyrolysis of petroleum pitch, which is the residue from the distillation of petroleum fractions. Cokes are

also products of pyrolyzed coal-tar pitch and pyrolyzed aromatic hydrocarbons at 300-500 °C. Carbon black, pyrocarbon and carbon films are examples of gas-phase pyrolysis products, *i.e*, products of thermal cracking of gaseous hydrocarbon compounds which are deposited as carbon on a substrate [19, 21]. It is also common to divide the non-graphitizable carbons into "soft" and "hard" carbons according to their hardness. Hard carbons contain nanopores.

1.4.3 Lithium-Graphite Intercalation Compounds

The synthesis of lithium-graphite intercalation compounds (Li_xC_6) is well known since the pioneering work of Hérold [22] in the mid 1950's. At ambient pressure a maximum lithium acceptance of one Li guest atom per six carbon host atoms can be reached in highly crystalline graphitic carbons, *i.e.*, "x" in Li_xC_6=1. The intercalation reaction proceeds *via* the prismatic surfaces (arm-chair and zigzag faces) of the host carbon. Intercalation through the basal plane can occur only at defect sites [23]. During the intercalation reaction the stacking order of the graphene layers in graphite shifts to AA stacking, *i.e.*, the intercalated lithium guests in Li_xC_6 are held between two carbon layers directly facing each other (Fig.1.5).

Due to intercalation of lithium the interlayer distance between the graphene layers is moderately increased (10.3% calculated for LiC_6) [24, 25]. The lithium intercalate interlayer stacking order is $\alpha\alpha$ leading to a Li-C_6-LiC_6-Li chain along the c-axis.

1.4.4 Anode Materials

In this section we will discuss on some practical carbon anode materials and their comparison studied by Sony Corporation [4]. Sony started its development of secondary lithium batteries with a metallic lithium anode in 1985 and batteries with a carbonaceous anode in 1986. It succeeded in the development of novel rechargeable lithium batteries with carbon anodes (the name lithium-ion secondary battery was given afterwards to this system) and introduced them in the market for the first time in the world in 1991. The carbon anode is the key component of the lithium-ion secondary battery, and various carbon materials ranging from graphite to amorphous carbon have been proposed. Although graphite is a passable material as an anode several drawbacks have been observed, including poor cyclability, limitation of capacity, and anode bulging. The Li doping capacity of graphite does not exceed 372 $mAh{\cdot}g^{-1}$, which is calculated from the stoichiometry of Li-GIC (LiC_6).

Thus, in order to improve the energy density of the battery, it is indispensable to develop carbonaceous materials which can be doped with more lithium than the stoichiometric limitation of Li-GIC. Graphitizable carbon (soft carbon) and non-graphitizable carbon (hard carbon) have been chosen as candidates for the anode materials of lithium-ion secondary cells in place of graphite.

Initial efforts was focused on soft carbon. This type of carbon has a considerably layered structure, as shown in Fig.1.7. Soft carbon can be easily converted to graphite by calcination at 3000 °C.

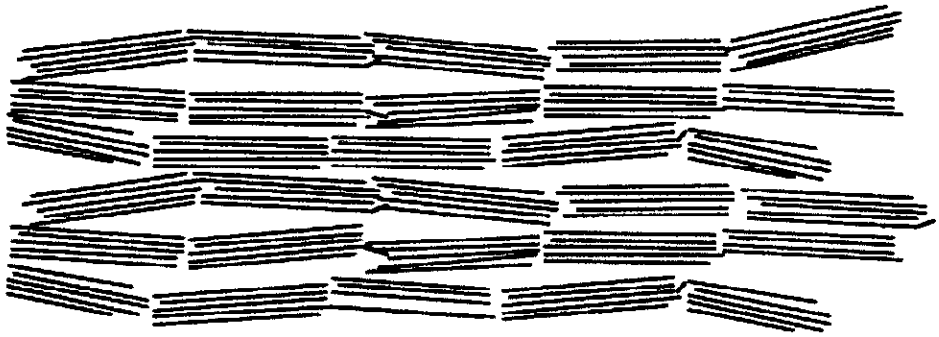

Figure 1.7: Schematic diagram of structure of soft carbon; Model of Franklin [14].

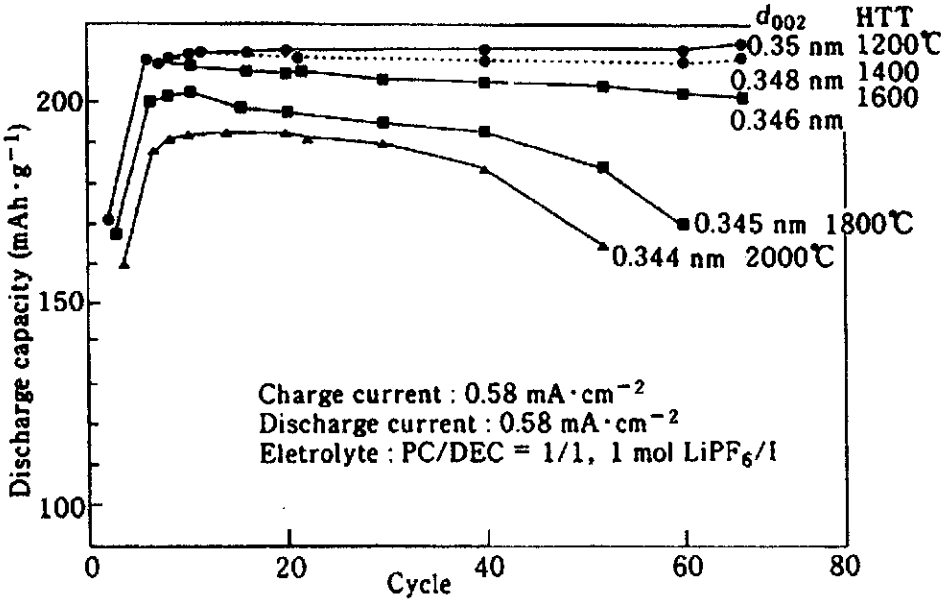

Figure 1.8: Effects of HTT and resulting d_{002} of soft carbon on discharge capacities of cokes; Y. Nishi[26].

Cokes prepared from petroleum pitch were heat-treated at various temperatures and their charge/discharge capacities and d_{002} spacings were determined. The results are shown in Fig.1.8 in which discharge capacities of the cokes studied in the electrolyte propylene carbonate (PC)/diethyl carbonate (DEC) with 1 M $LiPF_6$ are plotted as functions of the cycle number, d_{002} and heat-treatment temperature (HTT). It indicates that the lower the HTT, the broader the resultant d_{002} and the higher the discharge capacity of the cokes in the temperature range investigated.

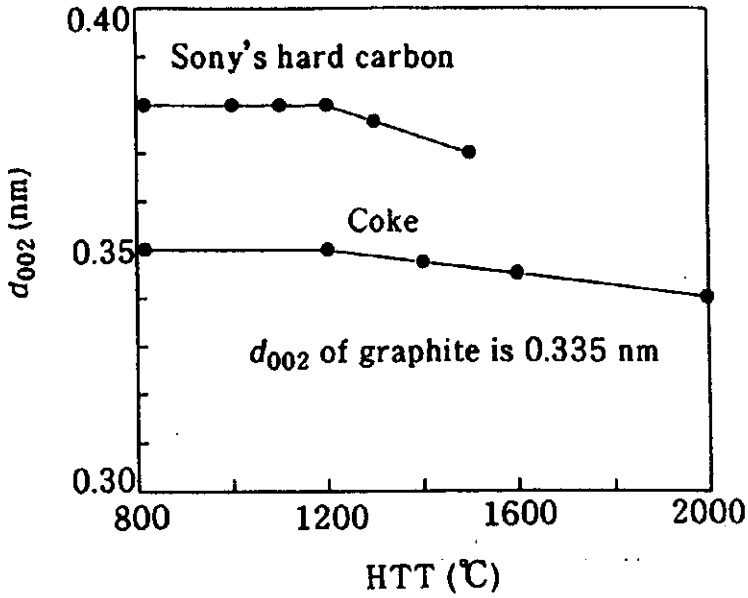

Figure 1.9: HTT dependence of hard carbon and soft carbon.
Y. Nishi [26].

Table 1.1: Effects of HTT on discharge capacity of PFA.
Y. Nishi [26].

HTT (°C)	Discharge capacity ($mAh \cdot g^{-1}$)
800	264
1000	311
1100	319
1300	312
1500	300

The results of the Fig.1.8 are likely to show that the morphology of soft carbon treated at higher temperatures approaches that of graphite and the electrolytes degrades simultaneously with lithium insertion, bringing about poorer cyclability. It is well known that d_{002} of graphite is 3.35 Å and while lithium intercalates between the layers, the d_{002} spacings expand up to 3.72 Å, then shrink back to 3.35 Å again by deintercalation of lithium. While soft carbon has slightly larger d_{002} spacings than graphite, it is still significantly narrower than 3.72 Å and soft carbon does not get rid of the expansion and contraction of d_{002} spacings due to lithium insertion and extraction.

It was assumed from the above results that carbonaceous materials with d_{002} spacings larger than 3.72 Å could be smoothly doped without expansion of the spacings and could be doped with much more lithium than graphite. Thus interest grew towards hard carbon with much larger spacings than graphite and soft

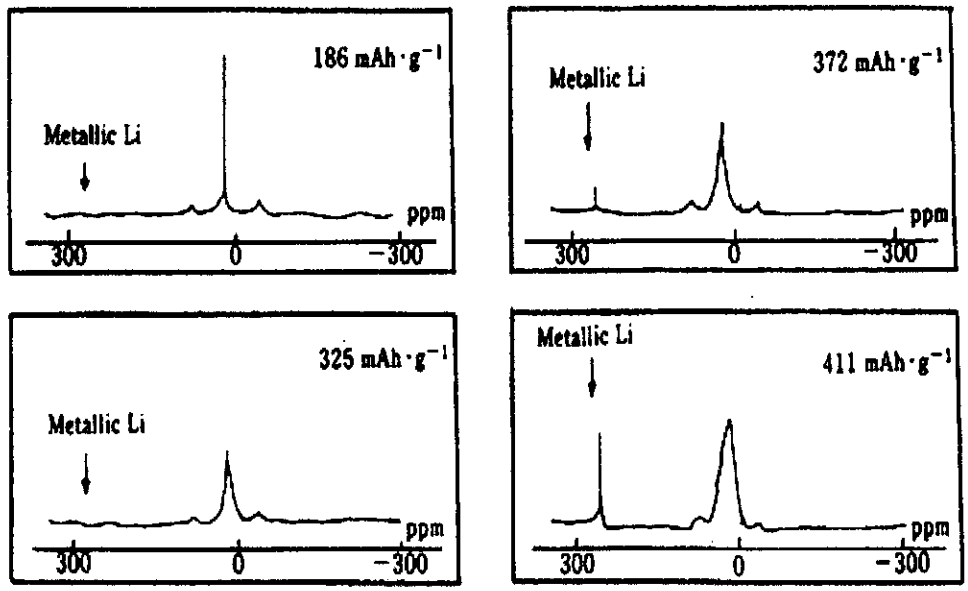

Figure 1.10: ^{7}Li-NMR spectra of graphite doped with varying amounts of lithium. Y. Nishi [27].

carbon. Hard carbon materials were prepared by carbonizing polyfurfuryl alcohol (PFA) resin at various temperatures, and charge/discharge of resulting carbons were determined as well as d_{002} spacings. Discharge capacities of PFA hard carbon prepared at various HTT's are shown in Table 1.1. Comparison of Table 1.1 with Fig.1.8 indicates that the discharge capacity of hard carbon is much higher than that of soft carbon. In Fig.1.9, d_{002} spacings of PFA carbon are compared with soft carbon as a function of HTT and it is clear seen from this figure that d_{002} spacings of this carbon, being over 3.72 Å at temperatures below 1500 °C, are considerably larger than those of soft carbon.

^{7}Li-NMR analysis was applied to graphite and hard carbon doped with various amounts of lithium. The results are shown in Fig.1.10 and 1.11. In these experiments knight shift of metallic lithium was taken as 265.7 ppm. In graphite (Fig.1.10) doped with lithium equivalent to less than 372 mAh·g^{-1}, a knight shift peak corresponding to metallic lithium does not appear. A tiny peak of metallic lithium is observed when lithium doping reaches 372 mAh·g^{-1}, which is equivalent to lithium content in LiC_6, and the height of the peak rises as the amount of doped lithium increases beyond the value of 372 mAh·g^{-1}, which means all the excess lithium deposits on the surface of graphite as metallic lithium.

On the other hand, in the case of hard carbon, lithium retention capability is much higher than that of graphite, as shown in ^{7}Li-NMR data on the hard carbon (Fig.1.11). No peak of metallic lithium can be observed even when hard carbon is charged to 450 mAh·g^{-1}. A small peak appears for the first time at 500 mAh·g^{-1} charging. It is assumed that this outstanding feature of hard carbon is due to the morphological differences between graphite and hard carbon. Graphite has an orderly layered structure and lithium can intercalate only into the spacings

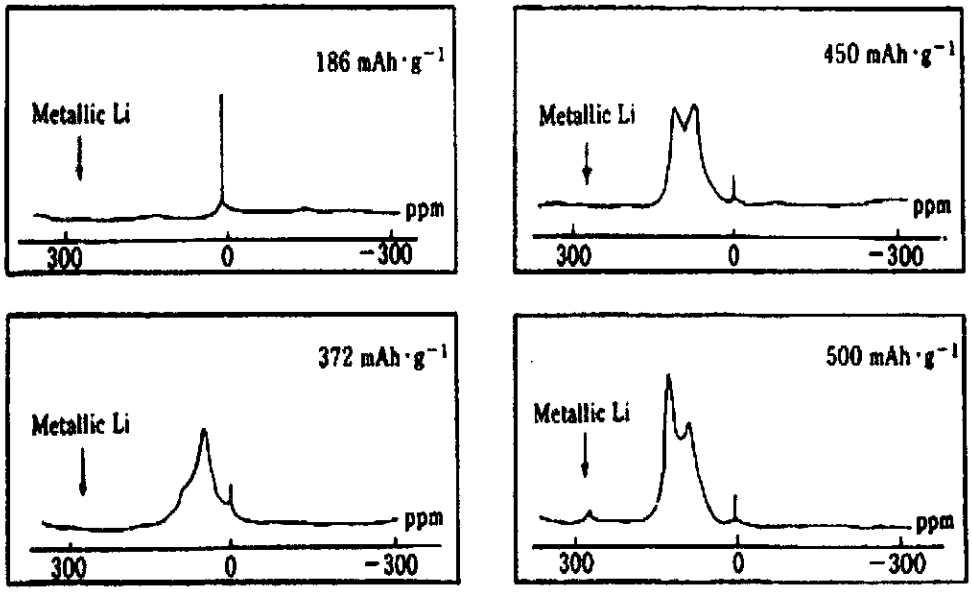

Figure 1.11: ^{7}Li-NMR spectra of hard carbon doped with varying amounts of lithium. Y. Nishi [27].

between these layers to form LiC_6, and soft carbon, which has a slightly disordered structure, is assumed to behave like graphite. On the other hand, hard carbon consists of randomly oriented small crystallites and this type of carbon can not be converted to graphite by calcination even at 3000 °C, which is the reason why hard carbon is called non-graphitizable carbon.

In the case of hard carbon, lithium can be electrochemically inserted into the ultramicropores (with diameter of about 8 Å) surrounded by these crystallites as well as the layers of crystallites themselves (Fig.1.1). The lithium doping capacity of these crystallites is subject to the stoichiometry of LiC_6 (372 mAh·g^{-1}), but as lithium trapped in the ultramicropores can also be discharged, the stoichiometric capacity limitation of hard carbon as a whole can be eliminated. In fact, a charging capacity of around 600 mAh·g^{-1} has been achieved in the hard carbon anode by optimizing the carbonizing conditions, and this value exceeds the stoichiometric limitation of Li-GIC.

Overcharge of a cell exceeding the designed voltage limits may result in the undesirable formation of lithium with high surface area on the anode surface. Thus, the large lithium doping capability of hard carbon is favorable for safety because of the larger margin until lithium deposition on carbon.

Hard carbon is very stable during charge/discharge cycles. This stability is due to the larger spacings between layers. As described above, during charge and discharge cycles, graphite and soft carbon repeatedly expands and shrinks. The graphite structure is damaged by this repeated expansion and contraction of spacings between layers, resulting in rapid capacity fade during cycles.

Chapter 2

Experiment

2.1 Overview

High-resolution small angle neutron scattering (SANS) and neutron powder diffraction (NPD) experiments were carried out on several different types of carbon used as anodes in secondary lithium-ion batteries. The materials selected were hard carbon, meso-carbon microbeads (MCMB), and Swedish natural graphite (crude and jet-milled). SANS data revealed nanopore structure in hard carbon. Absolute calibration of SANS data for hard carbon was done to calculate the volume fraction of nanopores. Estimation of the hexagonal (AB) and rhombohedral (ABC) phase content in Swedish natural graphite from NPD data revealed that the jet-milling increased the amount of ABC phase. In-situ X-ray diffraction (IXRD) technique was also used to see the staging phenomena during electrochemical intercalation of lithium into graphite anode. All these results are discussed to explain the electrochemical performances and structure-property relation of different carbon anode materials. The SANS and NPD data were collected using time of flight (TOF) instruments SWAN and VEGA respectively at the KENS pulsed spallation neutron source of the High Energy Accelerator Research Organization (KEK), Tsukuba, Japan. IXRD experiments were also carried out in the same facility.

2.2 Novelty of SANS

Gas adsorption techniques represent what are perhaps the most common approach to the characterization of the pore structure of the porous materials. Within this general area, the most popular technique by far is to derive surface area and pore size distribution information from nitrogen adsorption isotherms obtained at 77 K. Surface areas are most typically obtained from BET analyses (multipoint or single point), and pore size distributions from a number of different techniques based on various adaptations of the Kelvin equation, such as the BJH [28] and DM [29] approaches. A number of different approaches have been proposed for nanopore analysis, although it appears that no single technique is applicable to all situations. These range from nanopore volume determinations using the so-called

t-plot and alpha-plot methods, involving comparisons of experimental isotherms to standard isotherms, to pore size distribution determinations based on nanopore-filling arguments, such as those related to the Dubinin-Rasushkevitch equation, and others, like the Horvath-Kawazoecite [30] and density functional theory [31] methods. Often, pore size distribution determinations based on nanopore filling arguments use CO_2 adsorption at 273 K, to circumvent activated diffusion problems which may be encountered by nitrogen at 77 K in the smallest nanopores (i.e., the ultrananopores).

The theoretical limitations of these techniques are well documented and often different techniques result in nanopore size distributions which may differ significantly from one another. This state of affairs can be inadequate for a number of potentially important applications of microporous carbons; *e.g.*, for methane storage, for which it has been shown theoretically [32] that adsorption is a strong function of pore size.

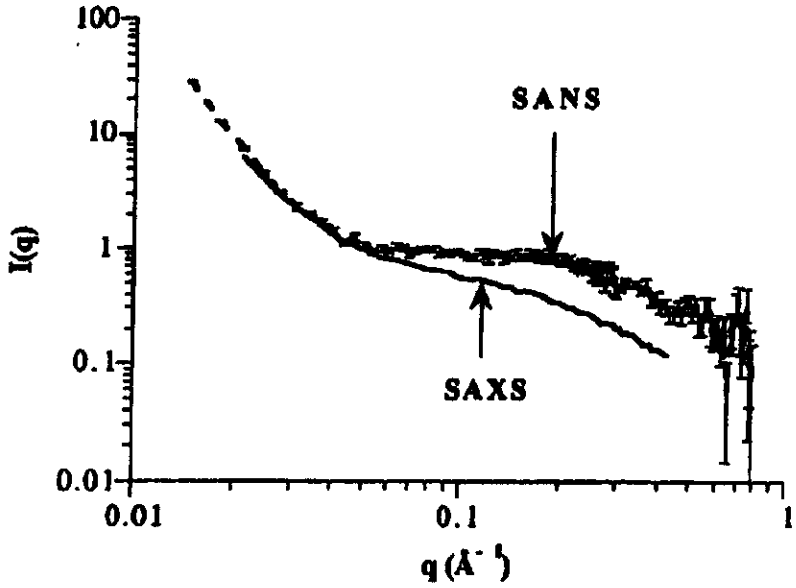

Figure 2.1: A comparison of SAXS and SANS for the phenolic resin char [33].

Small angle scattering (SAS) techniques represent an alternative to gas adsorption methods, with a number of advantages. SAS is sensitive to both closed and open porosity and in many cases offers a more complete picture of porosity. SAS can also be applied to wet samples. The most common subatomic scattering particles used in SAS are X-rays and neutrons, which can both be produced at suitable wavelengths for small angle scattering analyses. The generally greater accessibility to, and availability of X-ray instruments has made small angle X-ray scattering (SAXS) more common than small angle neutron scattering (SANS). But SANS is more efficient and accurate because scattering contrast between solid material and pore is more for neutrons resulting in higher intensity for SANS in the pore size range (high Q) than SAXS (Fig.2.1).

2.3 Instruments

2.3.1 Small/wide angle neutron diffractometer (SWAN)

The insrument SWAN stands for small/wide-angle neutron diffractometer. It was installed at the spallation pulsed-neutron source of KENS in KEK. SWAN utilizes C1 beam-line and the incident neutrons having a wide wavelength band from a solid methane moderator at 26 K, and was designed to cover a wide momentum-transfer (Q) range of 0.005 $\text{Å}^{-1} \leq Q \leq 12$ Å^{-1} with a high intensity. The available Q range of SWAN is 0.008 $\text{Å}^{-1} \leq Q \leq 2$ Å^{-1} [9].

Fig.2.2 schematically shows the layout of SWAN. The moderator-to-sample distance (L_i) is 13.2 m that gives a optimized resolution and intensity of SWAN. A point-collimator system is used without a vender or filter in order to make a use of wide range of neutron wavelength. SWAN has three banks of detectors to detect neutrons from three different Q ranges. The small-angle detector bank ($0.25° \leq 2\theta \leq 6°$) consists of 64 ^{3}He linear Position Sensitive Detectors (PSD's). The distance of the sample to the detector (L_f) for the small-angle bank can be varied from 2.3 m to 5.3 m. The available range of the neutron wavelength is $1 \leq \lambda \leq 11.3$ Å, with a small-angle detector bank at the 4.3 m position. The medium-angle detector bank ($12° \leq 2\theta \leq 20°$) is used for measurements in the Q range of 0.1 $\text{Å}^{-1} \leq Q \leq 2$ Å^{-1} and is arranged as eight-fold symmetry 1.1 m from the sample position. This bank consists of 48 conventional-type ^{3}He detectors. For the high-angle detector bank ($35° \leq 2\theta \leq 155°$) at 0.5 m from the sample position, 160 ^{3}He linear PSD's will be installed in the near future. Resolution, $\Delta Q/Q$, for this instrument is 0.3 at 0.005 Å^{-1}.

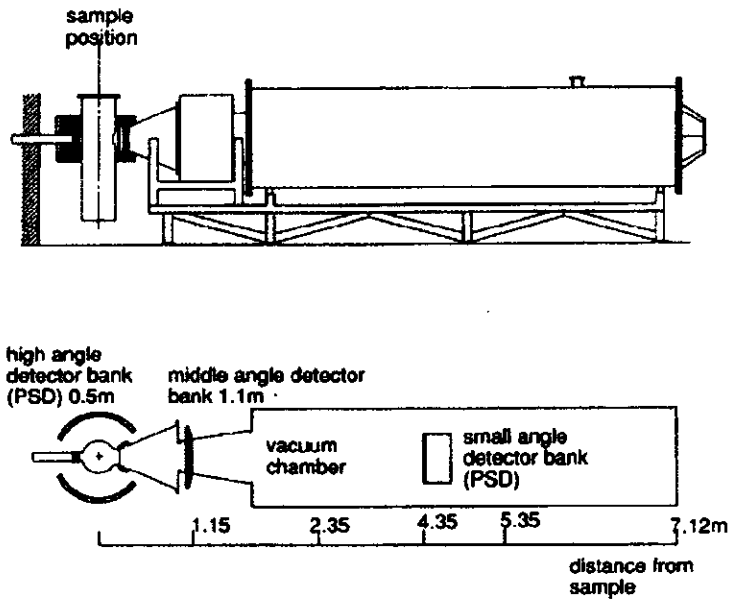

Figure 2.2: Schematic diagram of SWAN [9].

Initially the PSD system currently used for SWAN was originally developed for powder diffractometers at KENS [34]. Histograms of time-of-flight (TOF) spectra are stored in RAM of personal computers via VME modules in order to realize flexible position and time resolution of the detector of the PSD. Since these parameters are not necessary to be as flexible as powder diffractometers for SWAN, the VME module is modified to store TOF spectra in an on-board 1 MB memory on a VME module for 4 PSD's by a field programmable gate array (FPGR). Instrument-control software is developed by the application LabView^{TM} (National Instruments Corporation) to make it user-friendly. Data analysis code (SWAIN) is developed in ANSI-C. Although this code is executed on Macintosh and HP workstations, it is now easy to import to other platforms. SWAN produces several thousands of TOF spectra for one measurement, and the statistics of each spectrum is generally poor. This means that it is essential to merge pixels in the best way for each experiment. The development of a visualization software combined with the analysis code SWAIN is in progress. As a first step, the "ISIS raw-data" format is chosen, since this is a standard format at KENS. File-conversion software for a new format, NeXus, is under davelopment which is proposed by international collaboration team. NeXus is an application based on the HDF format, and many commercial software programs supporting HDF can read NeXus files without any development of additional software.

2.3.2 Neutron Powder Diffractometer (VEGA)

VEGA is a high-resolution time-of-flight neutron powder diffractometer with three banks of one-dimensional position-sensitive detectors (PSD's) at KENS facility. It has been designed on the basis of the following principles and/or criteria [35].

(1) To enhance the efficiency of data collection, an increase in the detector solid angle without sacrificing resolution is indispensable.

(2) A 90° bank is useful for measurements under special environments such as high pressure or high temperature. To obtain reliable structural data, a resolution, $\Delta d/d$, of at least 5×10^{-3} is necessary. Textures and residual strain under special environments can also be studied with this bank.

(3) To cover a wide range of d-spacing, a low angle bank is indispensable. It provides us with low-Q intensity data to analyze magnetic structures and crystal structures with large unit cells. This bank is also suitable for indexing problems.

(4) A back-scattering bank is required for conventional structure refinements. A solid angle much larger than that of HRP, the previous powder diffractometer at KENS [36], should be attained in this bank.

As shown in the illustration (Fig.2.3) VEGA consists of three detector banks comprising one-dimensional ^{3}He position-sensitive detectors (1D-PSD's). Each PSD has a diameter of 1.27 cm and an effective length of 60 cm, containing 10 atm of ^{3}He with appropriate stopping gases. The important parameters of VEGA are listed in Table 2.1.

PSD's are used to satisfy the principle (1) because of the following reason: In the backscattering and 30° banks, arrangement of many short and long normal

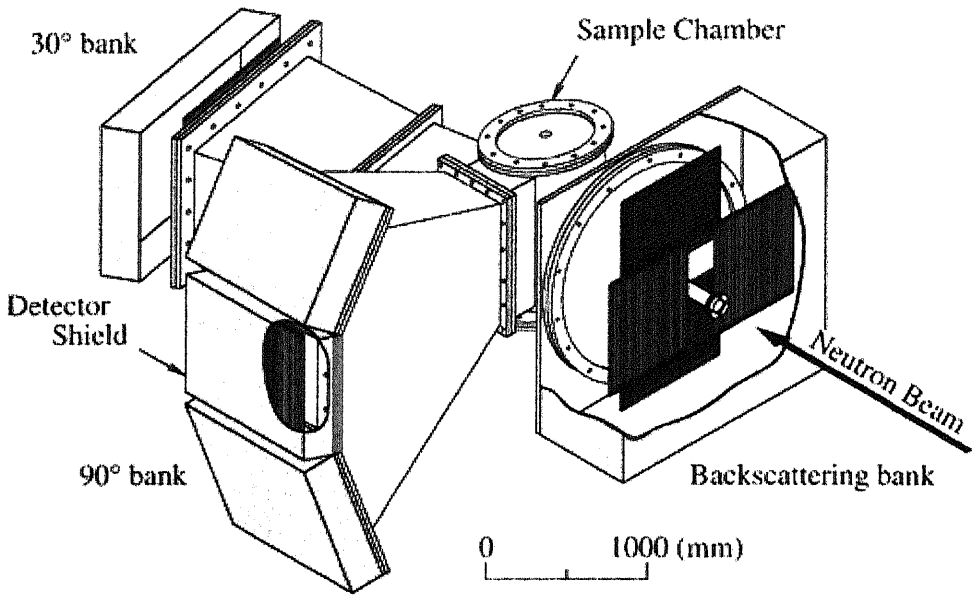

Figure 2.3: Three-dimensional view of TOF powder diffractometer VEGA [35].

detectors along the Debye-Scherrer rings inevitably produces wide inactive regions; By adopting PSD's, this can be minimized without sacrificing resolution. PSD's are also better than normal detectors in studies on textures and residual strain with the 90° bank. In principle, two-dimensional PSD's (2D-PSD's) are preferred to 1D-PSD's. Nevertheless, the arrays of 1D-PSD's were adopted in VEGA because of their higher counting-rate limitations and simpler maintenance than those of 2D-PSD's. As shown in Table 2.1, the backscattering bank covers a solid angle of 1.2 str with a resolution of $\Delta d/d = 2\times10^{-3}$. In comparison with HRP (solid angle is 0.14 str), SEPD (0.09 str) at IPNS [37] and HRPD (0.31 str at 1 m position) at ISIS [38], a large increase in the solid angle is realized without any sacrifice of resolution.

The 90° bank comprises three sub-banks arranged vertically. This increases not only counting rates in powder diffraction experiments but also the data collection efficiency in texture studies. The solid angle of the 90° bank is about three-times as large as those of HRP, SEPD and HRPD.

In the low-angle bank with an average 2θ of 30°, the resolution of each detector segment differs significantly, depending largely on 2θ of the segment. We can change the range of detector segments grouped into one data to adapt it for experimental purposes.

VEGA has several features that favor its applications to various types of neutron diffraction experiments. High-resolution single-crystal diffraction is one of the promising applications of VEGA. The TOF method using the PSD's enables us to scan wide reciprocal space simultaneously. Fine structures of Bragg reflections due to crystalline imperfection, diffuse scattering and their changes with temperature can easily be observed.

Table 2.1: Instrumental parameters of VEGA with measured values of resolution. Moderator: solid methane at 20 K. Incident flight path: 20 m. L_2: scattered flight path. Figures in parentheses are numbers of PSD's which have already been installed [35].

Parameters	Back Scattering	90°	30°
L_2	1 m	2 m	2 m
No. of PSD's	216(64)	144(0)	72(16)
2θ	140-175°	81-99°	20-40°
d-spacing	0.5-4Å	0.6-6Å	1-20Å
Solid angle	1.2 Str	0.27 Str	0.14 Str
Resolution	2×10^{-3}	5×10^{-3}	8×10^{-3}

The PSD-VME data-acquisition system adopted in VEGA involves a VME single-board computer with the 68040 processor for data handling. The position-encoding method in this instrument is nearly the same as that in the GLAD diffractometer for glass, liquids and amorphous materials at IPNS [39, 40] but its data-transfer and histograming system has been developed independently at KENS.

This system has several features to facilitate the tuning of encoder modules. For example, the feature that allows measurement of pulse-height spectra from all PSD's is used extensively in initial adjustments of the encoder modules. A feature for generating pulses to test the whole electronics system (PSD tester) is also implemented. The encoded data are transferred immediately through the VME bus and histogramed in a fashion defined in several lookup tables. Each event can be binned in several different spectra by multiple histograming. On-the-fly time-focusing is routinely carried out using this feature.

2.4 Experiment on Graphite

In this study we investigated Swedish natural graphite of high purity (99.8%) Woxna (**W**) (Tricorona AB) by SANS, NPD and IXRD experiments. Results from both crude and three jet-milled Woxna graphites (**A1**, **A2**, and **A3**) are presented. The jet-milling was done by our collaborator on a alpine fluidized bed opposed jet-mill 100 AFG at a speed of 22000 rpm [41]. An Al_2O_3 wheel was used with three nozzles of diameter 1.9 mm. The nozzle supply pressure, time duration, and the amount of sample were varied for the different batches.

For IXRD experiment the top cover of the in-situ cell was specially designed. As shown in Fig.2.4, with the flat surface we did not have any information of Bragg reflections with 2θ less than 28° because the 2 mm thick steel plate had a shadow effect on the graphite electrode for the incoming X-ray beams. Eventually we are much interested in this range to see the 002 Bragg reflection from graphite

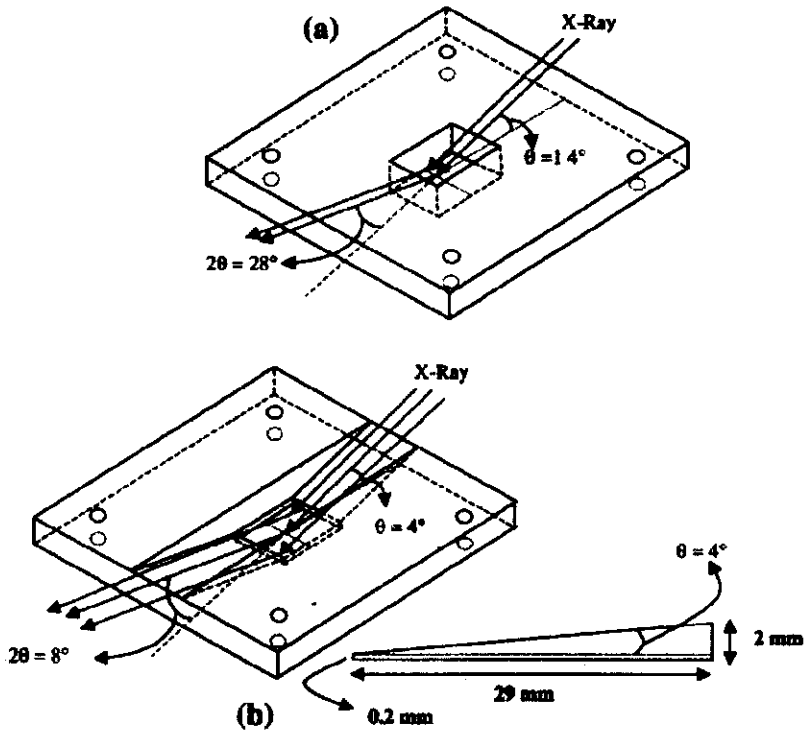

Figure 2.4: Detail construction of the top cover for the in-situ cell.

layers. To remove the shadow a slope was cut which started from the surface at the outer sides in the direction of incoming and outgoing X-ray beams and ended with the sharp edges at the center sides. This allowed us to have information down to 2θ=8°. Woxna graphite electrode was used to construct the electrochemical cell. The electrode mixture is 80% graphite, 10% carbon black and 10% EPDM-binder [42]. The cell was galvanostatically discharged from fresh cell (V_{oc}=2.85 V) to three different voltage levels (0.30 V, 0.18 V and 0.15 V). To ensure the electrochemical equilibrium at each level the cell was kept at potentiostatic mode for few hours until the current flow inside the cell went down to 10 μA. Then IXRD experiments were carried out at the end of each level to see the structural change and staging phenomena within graphite layers.

2.5 Experiment on Soft Carbon

To study the structure of soft carbon SANS and NPD experiments were carried out on MCMB (SGB-II, SEC). Electrochemical cycling was also done in the in-situ cell. The in-situ cell has been constructed and its internal construction is shown in Fig.2.5. It is basically a half cell where Li metal is used as reference and counter electrode and carbon anode as the active material. The electrode mixture is 90.5% carbon (MCMB) and 9.5% binder (PVDF). This paste like mixture is coated on

a 2 μm thin Cu foil. The amount of carbon loading was 18.73 mg/cm^2. The Cu foil acts as the current collector. Celgard 3401 (25 μm) membrane was used as the separator. It uses a combination of two surfactants to produce rapid and complete pore wetting in high surface tension liquids. Few drops of electrolyte of 1 mol·dm^{-3} solution of $LiPF_6$ in a 50:50 (by volume) mixture of EC and DEE was put on the separator to wet. The complete cell was prepared in argon filled glove box. Galvanostatic discharging and charging was done by a galavanostat at 1 mA current rate which is below C/10 value. A precision digital voltmeter was connected to the external terminals of the in-situ cell to observe the instant voltage. To plot the discharge/charge curve, voltage and time data were recorded by interfacing the voltmeter with the computer through a General Purpose Interface Board (GPIB). LabView^{TM} (National Instruments corporation) application was used for data acquisition.

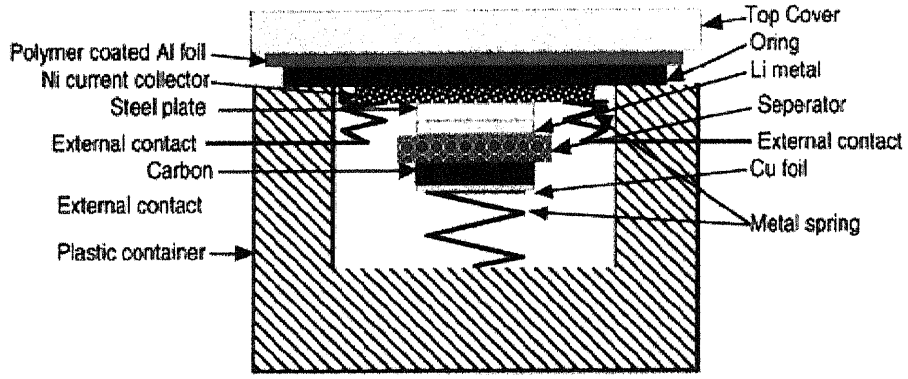

Figure 2.5: Construction of in-situ cell.

2.6 Experiment on Hard Carbon

Carbon fiber prepared from an isotropic petroleum pitch (nominal diameter of 10 μm, FIP, Petoca Ltd.), a precursor of non-graphitizable carbons, was heat-treated at 1200 °C. Electrochemical Li insertion was performed in a three-electrode cell with 1 mol·dm^{-3} solution of $LiPF_6$ in a 50:50 (by volume) mixture of ethylene carbonate (EC) and diethylcarbonate (DEC) at 27 °C. The reference and counter electrodes were Li metal. Carbons are lithiated with two different concentrations of Li called partially lithiated carbon ($LiC_{10.4}$) and fully lithiated carbon (LiC_5). Both $LiC_{10.4}$ and LiC_5 were prepared by galvanostatic reduction. The fully lithiated carbon was prepared by short circuiting the cells for 12 h after galvanostatic reduction (25 mA·g^{-1}) to 0 V.

To investigate the nanopore-structure in the hard carbon SANS experiment was carried out on carbon fiber sample. Then the sample was partially lithiated and another run was carried out to see the change in the structure. Finally carbon fiber was fully lithiated and final run was done.

Low temperature experiment was also carried out on fully lithiated carbon fiber. Cryostat cooling was used to cool down the sample chamber to 96 K. A temperature controller was connected to the cooling system to maintain a stable temperature at the desired level.

Chapter 3

Results and Discussion

3.1 Comparison of SANS data for hard carbon, soft carbon and graphite

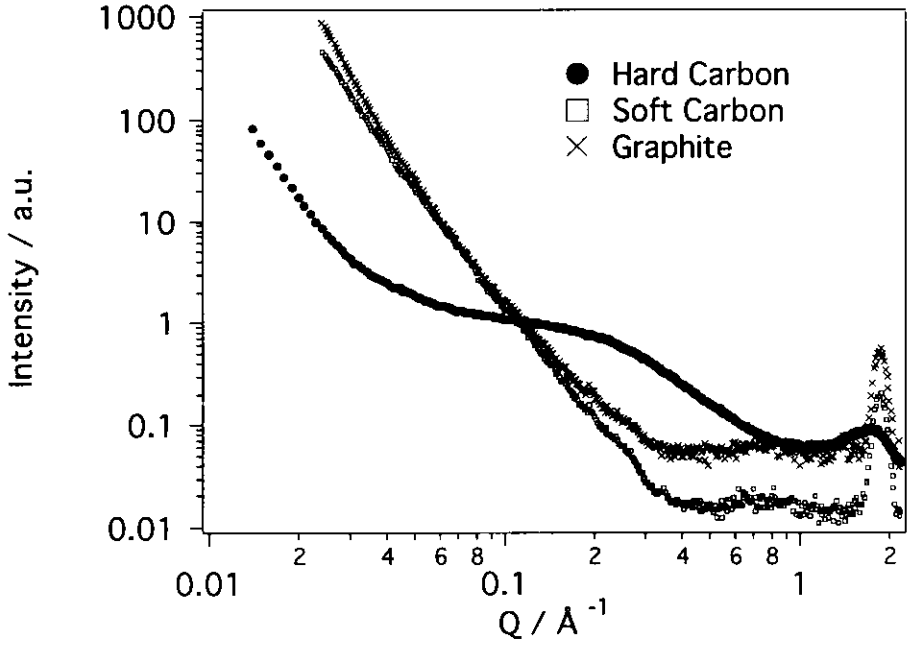

Figure 3.1:SANS data for hard carbon, soft carbon (MCMB) and jet-milled Swedish natural graphite (A1).

3.1.1 Hard Carbon (Carbon fiber)

Fig.3.1 illustrates the scattering profile of SANS data for graphite, soft carbon and hard carbon. It is seen in the scattering profile of hard carbon (carbon fiber) that a big shoulder exists in the region 0.1 $Å^{-1} < Q < 1.2$. This extra scattering is

responsible for the contrast between carbon matrix and nanopores. This confirms about the existence of nanopores. Details about pore information is stated later in this chapter. A broad 002 Bragg peak in the high Q region indicates disordered structure of hard carbon.

3.1.2 Soft Carbon (MCMB)

In many literature it is established that soft carbons like MCMB contain both graphitic and turbostratic structure. In the turbostratic region, graphite sheets are randomly stacked and pinned to each other. Therefore, the arrangement of the graphite planes into A—Li layer—A requires much energy to intercalate lithium. T. Kasuh *et al.* [43] calculated the projected probability function and measured (hk) XRD peaks of MCMB to simulate turbostratic structure in adjacent to parallel two graphite layers. Turbostratic disorder is responsible for the creation of crystal defects which might be additional sites for lithium storage. To investigate about the existence of nanopores in our MCMB sample small angle neutron scattering (SANS) experiment was carried out. Unlike hard carbon no shoulder was found in the scattering curve of MCMB indicating no nanopore-structure (Fig.3.1).

3.1.3 Graphite

Woxna (**W**) is the crude Swedish Natural Graphite. Various kinds of milling, in three different batches **A1**, **A2** and **A3**, have been applied to influence the structure and the capacity of Woxna. The milling conditions used in this study are shown in Table 3.1. Jet-milling introduced increased capacity and stable cycle performance. It was suspected that jet-milling might introduce some nanopores in the sample but as illustrated in Fig.3.1, no nanopore-structure was observed in the jet-milled graphite. The same result was found in all three jet-milled graphite samples. We can conclude that crude Swedish natural graphite does not have any nanopore content and jet-milling does not introduce nanopore.

Table 3.1: Conditions for jet milling of Woxna (W), A1, A2 and A3 represents three different jet milled Woxna graphites; M. Herstedt [41].

Condition	A1	A2	A3
Pressure [bar g]	6	4	2
Air consumption [Nm^3/h]	40	30	18
Test duration [min]	11	10	15
Throughput rate [Kg/h]	2.1	2.0	0.8

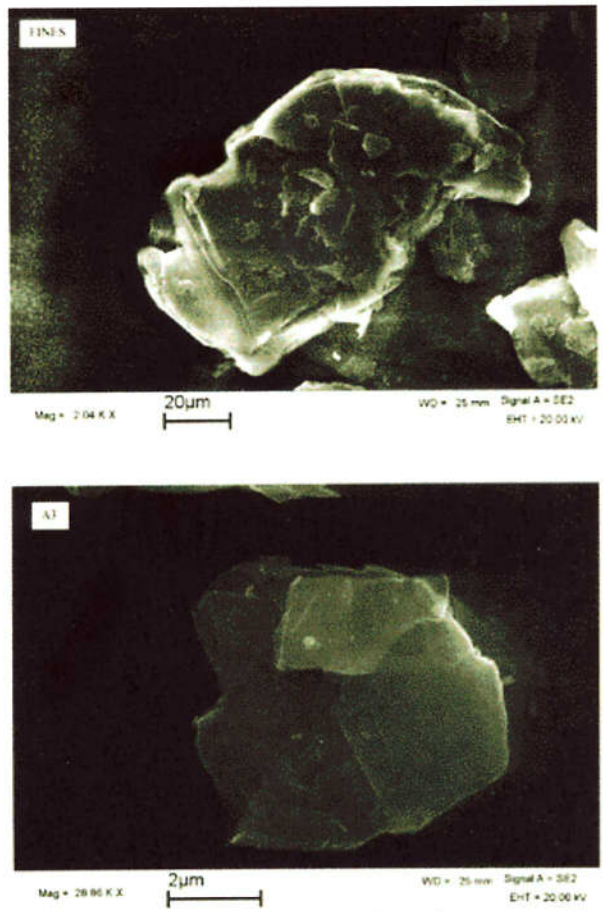

Figure 3.2: Scanning electron microscope (SEM) picture of crude (top) and jet-milled (bottom) Swedish natural graphite; M. Herstedt [41].

3.2 Effect of Jet-milling on graphite

Fig.3.2 shows scanning electron microscope (SEM) picture of crude Swedish natural graphite (Woxna fines) and jet-milled sample. Table 3.2 shows some physical and electrochemical properties of Swedish natural graphites (crude and jet-milled). Jet-milling made the graphite particle size smaller, and hence increased the specific surface area (BET) as shown in Table 3.2. Particle size distribution of jet-milled samples is also illustrated in Fig.3.3. The irreversible capacity increases with BET as expected since it is related to the decomposition of solvent on the graphite surface to form a Solid-Electrolyte-Interface (SEI) layer. It seems that there is no relation between BET and reversible capacity.

All jet-milled samples **A1**, **A2** and **A3** provided increased capacity after jet-milling. So there must be a change in some structural parameter after jet-milling. Neutron powder diffraction (NPD) experiment was carried out to explore this change. Comparing the calculated scattering pattern from hexagonal (AB) and rhombohedral (ABC) phase with observed pattern it is evident that Woxna graphite (**W**) contain both AB and ABC phase (Fig.3.4). Similar results were found for **A1**,

Table 3.2: Properties of Swedish natural graphite; M. Herstedt [41].

	Size [μm]	BET m^2/g	Reversible Cap. 1^{st} cycle [mAh/g]	Irrev. Cap. 1^{st} cycle [%]
W	>80	3.77	340	17
A1	8.0	10.91	371	24
A2	7.4	12.66	371	28
A3	6.6	12.75	350	29

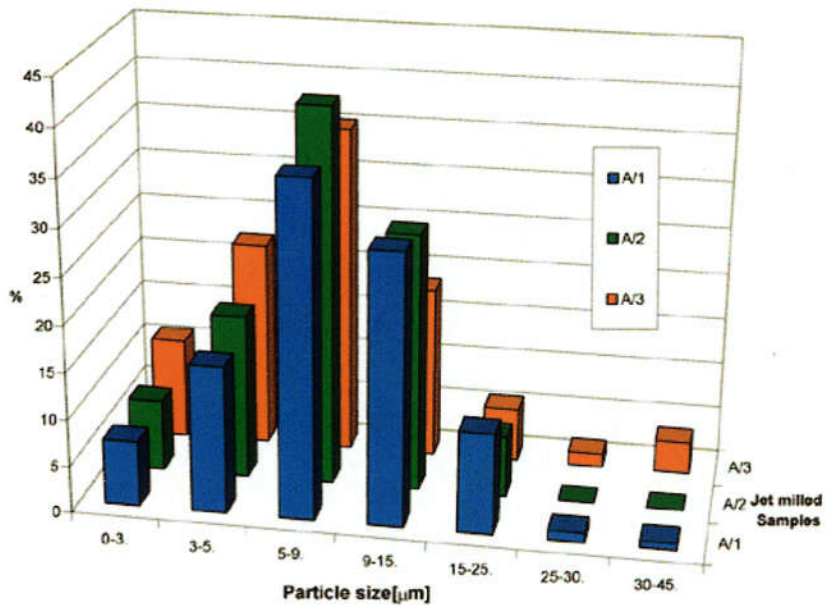

Figure 3.3: Particle size distribution of jet-milled Swedish natural graphites (A1, A2, A3); M. Herstedt [41].

A2, and **A3**. As a rough estimation the mass fraction of AB and ABC phase was calculated from NPD data (Table 3.3). It is clear that jet-milling of graphite not only reduces the particle size but also increases ABC phase content at the expense of AB phase. Reversible capacity vs. ABC phase content is plotted in Fig.3.5, which indicates that the capacity increases with ABC phase content. It can be concluded that jet-milling increases the ratio of ABC to AB phase contents in Swedish natural graphite and increased rhombohedral (ABC) phase content gives higher capacity.

Some reasons have been suggested why increased rhombohedral phase improved reversible capacity [44, 45]. Firstly, more rhombohedral phase increases the defects on the basal plane along the boundaries between rhombohedral and hexagonal phases. These defects on the basal plane probably reduce the incorporation impedance of lithium ions into the graphite lattice leading to an enhanced kinetic process [44]. Secondly, the flake like particle shape of Woxna graphite might be

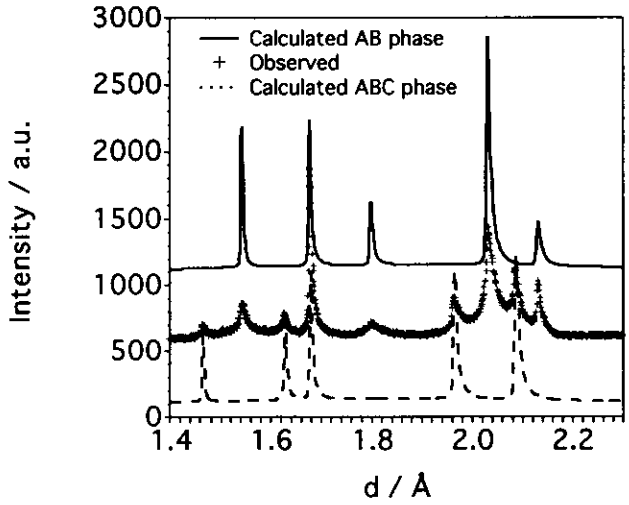

Figure 3.4:NPD data for Woxna graphite (**W**), calculated AB and ABC phase are offset for clarity.

Table 3.3: AB and ABC phase content in Swedish graphites

	A1	A2	A3	Woxna
Hexagonal (AB) phase[%]	58	58	62	82
Rhombohedral (ABC) phase[%]	42	42	38	18

changed to potato shape after jet-milling. Potato shape reduce the basal plane surface area, consequently, reducing the exfoliation of graphite surface, and hence increase reversible capacity [45].

As for the cycling performance of graphite electrodes, reversible capacity of jet-milled graphites are relatively stable while that of Woxna increased with cycling and reached to the value of **A2** after 25th cycle [42](Fig.3.6). This might be attributed to the difference in surface morphology between crude and jet-milled graphite which affect the SEI layer formation.

Phase diagrams of lithium intercalation compounds are well probed using electrochemical methods and in-situ X-ray diffraction (IXRD) techniques [46, 47, 48]. In-situ X-ray diffraction experiment was carried out to observe staging phenomena in jet-milled graphite. Fig.3.7 shows the data of IXRD. Peaks from graphite 002 layers occured around 2θ=26°. Enlarged version of these peaks are illustrated in Fig.3.8. All the peaks from graphite layers are superimposed on a broad polymer peak. This polymer was used under the top cover of the in-situ cell to cover the window and make the cell air-tight. Peak A comes from the pristine graphite 002 layers (d=3.3637 Å) without lithium being intercalated. We call it "fresh cell" and the open circuit voltage (OCV) was found to be 2.85 V. Then lithium intercalation was started and OCV was gradually decreasing. At OCV=0.3 V second IXRD measurement was done. This time d-spacing increased to 3.3787 Å indicating lithium intercalation into graphene layers. In the third measurement (OCV=0.18 V) we

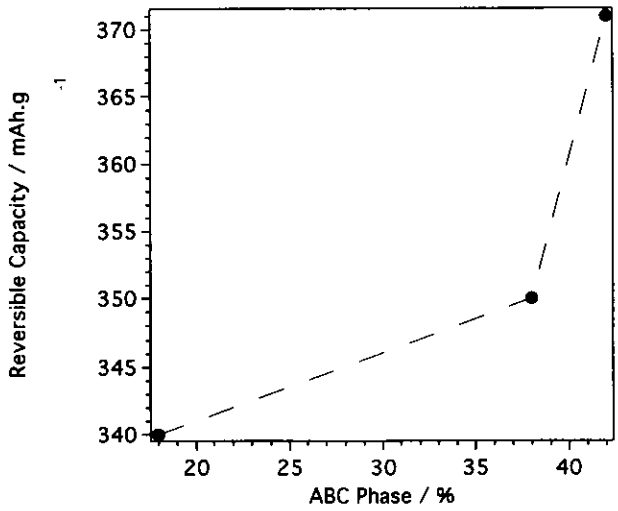

Figure 3.5: Reversible capacity vs. ABC phase content in graphites.

observed two peaks (C1 and C2). peak C1 at d=3.4041 Å represents diluted stage-1 phase where lithium intercalates into every layers. Peak C2 occured from stage-4 phase where lithium intercalation takes place in only one among four consecutive graphite layers. Therefore coexistence of two phase was observed. At OCV=0.15 V peak from diluted stage-1 disappeared and peak D appeared as a single phase of stage-4 with increased lithium concentration in staged layers resulting in higher average d value of 3.4613 Å.

The average interlayer distance, d_4, of the stage-4 phase was calculated by:

$$d_n = \frac{C_L + (n-1)C_0}{n} \tag{3.1}$$

where n is stage number, C_L denotes the thickness of one lithiated layer of LiC_6, 3.703 Å and C_0 means vacant interlayer distance of the natural graphite, 3.3637 Å. Although it was a rough estimation, the experimental data (d_4=3.4508 Å, peak C2) showed fairly good agreement with the calculated value (3.4485 Å).

3.3 Electrochemical cycling of MCMB

As shown in Fig.2.5 the in-situ cell has been constructed to perform electrochemical studies. The cell was galvanostatically discharged and charged for several days with MCMB (SGB-II, SEC) electrode using 1 mol·dm^{-3} solution of $LiPF_6$ in a 50:50 (by volume) mixture of EC and DEE as electrolyte. Fig.3.9 shows the discharge/charge curves for first three cycles between 1.5 V and 0.01 V. Since metallic lithium was used as the reference and counter electrodes, the MCMB electrode is positive in this <MCMB—Liquid Electrolyte—Li> cell system. Thus, we describe discharge for

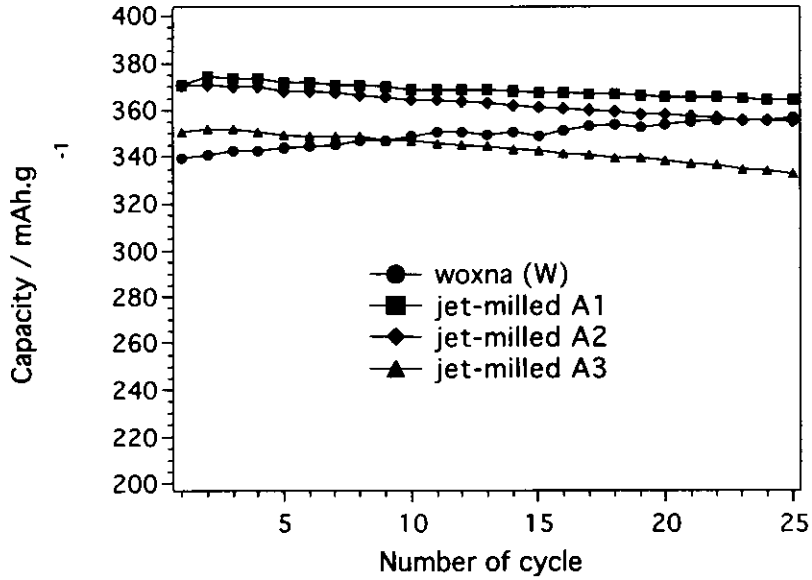

Figure 3.6: Electrochemical cycling of Swedish natural graphites; M. Herstedt [41].

lithium intercalation into the MCMB (cathodic reduction) and charge for lithium deintercalation (anodic oxidation).

During discharge in the first cycle the curve had a plateau at 0.9 V which is caused by the decomposition of solvent on MCMB grain surface to form passivation layer to stop further reaction. This layer is also called Solid-Electrolyte-Interface (SEI) layer. It inhibits electronic conduction but allows Li^+ transportation between electrolyte and MCMB grains. Efficiency at the first cycle is more than 95% which is a significant feature of this sample. It also showed a very long plateau near 0 V which is very useful for battery application. As for the cycling performance the reversible capacity was getting down and down with cycling. As shown in Fig.3.9 capacity decreased by 25% when compared the charging capacity in the first cycle with that of in the second cycle. It decreased by 16% between the second and third cycle.

3.4 Effect of Lithiation into Hard Carbon

Fig.3.10 shows SANS data obtained from SWAN for hard carbon, partially lithiated hard carbon ($LiC_{10.4}$) and fully lithiated hard carbon (LiC_5). In the range 0.1 $Å^{-1}$< Q <1.2 $Å^{-1}$ the curve shows a very big shoulder with flat tail which is the result of scattering from the voids superimposed with constant backgrounds. In the range 1.2 $Å^{-1}$< Q <2.0 $Å^{-1}$ we observed the 002 Bragg reflection from graphene layers. The broadening of the Bragg peaks is due to the disordered nature of the hard carbon. In the present work we focused on the shoulder and Bragg peak region to extract information about void sizes and 002 plane spacings before and after Li

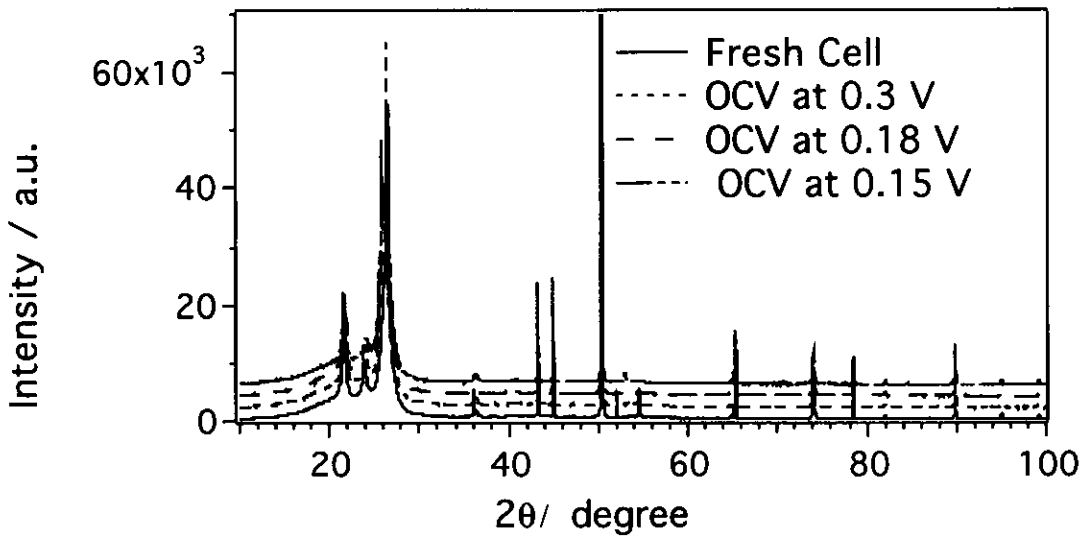

Figure 3.7: In-situ X-ray diffraction data for jet-milled graphite. Intensity at 0.3 V, 0.18 V, and 0.15 V were offset for clarity.

intercalation. Data is fitted by the following equation:

$$I = AQ^{-4} + \frac{I(0)}{\{1 + (\xi Q)^2\}^2} + Be^{\frac{-(Q-Q_0)^2}{\sigma^2}} + Bkg \tag{3.2}$$

Contribution to the scattering curve of individual components in the fitting equation (Eq.3.2) is shown in Fig.3.11. On the right side of Eq.(3.2), first term obeys Porod law. Tail part or the intensity at higher Q-region from any big structure or grain boundaries started decaying from 0.04 Å and overlaps with the initial part of the scattering from voids at around 0.07 Å. According to porod law the tail part should be proportional to Q^{-4}. Second term is Debye-Bueche function, third term is Gaussian function signifying Bragg contribution and the last term, *Bkg*, is for constant background. ξ is called correlation length which is related to the radius of gyration of the pores, Q_0 represents the position of the 002 Bragg peak produced by graphene layers, and $I(0)$ is the intensity extrapolated to $Q = 0$ in Debye-Bueche function and can be expressed as:

$$I(0) = n(\Delta\rho V_P)^2 \tag{3.3}$$

where n is the number density of pores, $\Delta\rho$ is the difference in scattering length density between matrix and nanopore, and V_P is the volume of nanopore [49].

For low Q region Debye-Bueche equation can be approximated as follows:

$$\begin{aligned} I &= \frac{I(0)}{\{1 + (\xi Q)^2\}^2} = \frac{I(0)}{1 + 2\xi^2Q^2 + \xi^4Q^4} \\ &\approx \frac{I(0)}{1 + 2\xi^2Q^2} \approx I(0)\{1 - 2\xi^2Q^2\} \end{aligned} \tag{3.4}$$

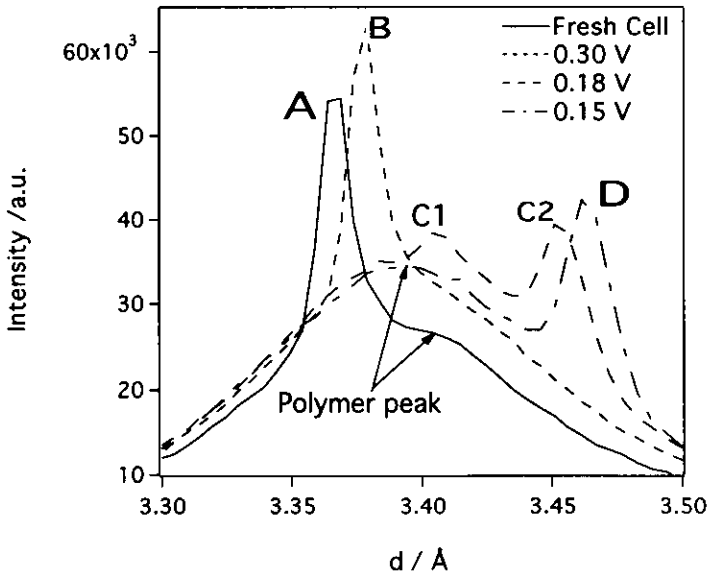

Figure 3.8: In-situ X-ray diffraction data of Bragg peaks from graphite layers.

For low Q region Guinier equation can be approximated as follows:

$$I = I(0)e^{-\frac{R_g^2Q^2}{3}} = I(0)\{1 - \frac{R_g^2Q^2}{3} + ...\}$$
$$\approx I(0)\{1 - \frac{R_g^2}{3}Q^2\} \quad (3.5)$$

Where R_g is the radius of gyration of the pores.

It is evident from equation (4.3) and (4.4) that the Debye-Bueche and Guinier equations become identical at low Q regions. Hence ξ and R_g can be related as

$$2\xi^2 = \frac{R_g^2}{3} \Rightarrow R_g = 2.45\xi \quad (3.6)$$

So from the value of ξ obtained from fitting result we can easily estimate the pore size.

Fig.3.12, 3.13, and 3.14 show the fittings for hard carbon, partially lithiated hard carbon ($LiC_{10.4}$), and fully lithiated hard carbon (LiC_5), respectively. Fitting results are shown in Table 3.4. Fig.3.15 shows the 002 Bragg peaks. Statistics of the data around Bragg peaks is not good for SWAN and d_{002} values in Table 3.4 is not considered highly accurate. It is obvious from Fig.3.15 that after partial lithiation distance between graphene layers increases and no significant change after fully lithiation. Neutron diffraction data obtained from VEGA were analyzed precisely to know the distance between graphene layers. Kanno *et al.* [50]

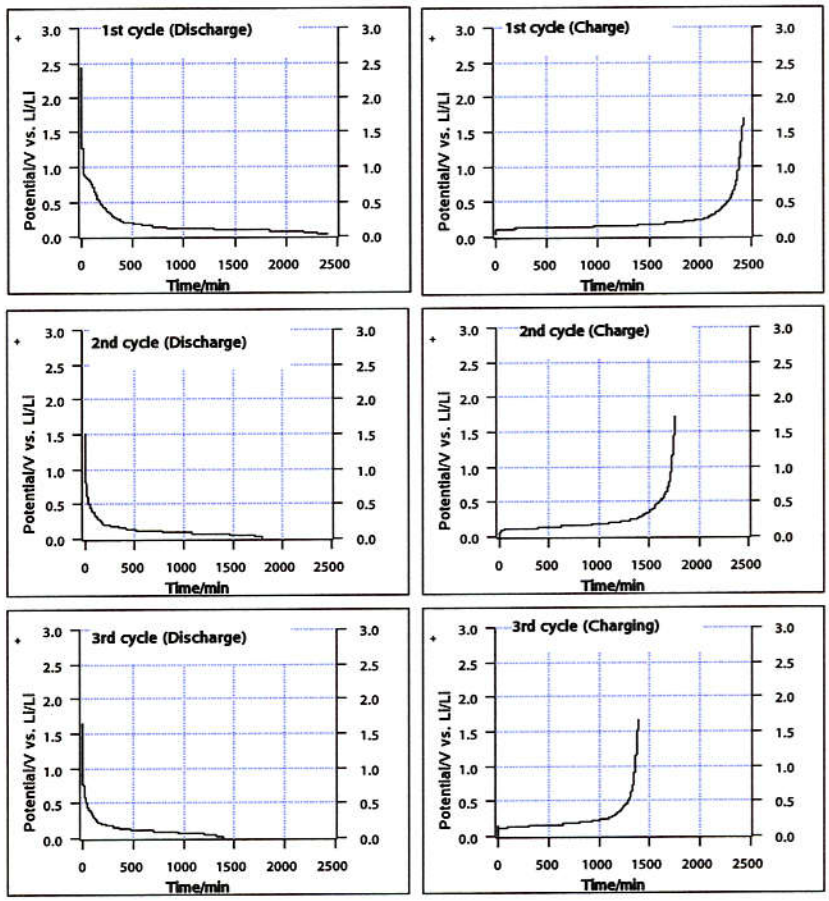

Figure 3.9: Discharge/charge (0.1 mA) curves of MCMB (SGB-II, SEC) electrode using 1 mol·dm^{-3} solution of $LiClO_4$ in a 50:50 (by volume) mixture of EC and DEE as electrolyte.

fitted VEGA data by the graphite-2H model with a hexagonal structure that led to lattice parameters with $a = 2.4064(7)$ Å, $c = 6.985(11)$ Å; and $a = 2.4186(6)$ Å, $c = 7.074(9)$ Å for carbon and lithiated carbon respectively. No significant differences were found in the peak positions between the fully and partially lithiated samples. This indicates that during partial lithiation Li-ions intercalates into the spacings between graphene layers and the 002 interplaner distance increases. When more Li go into the sample they do not go into the graphene layers. They go somewhere else.

Fig.3.16 shows that the shoulder shifts towards low Q for fully lithiated sample (LiC_5). But no significant shift for partially lithiated sample ($LiC_{10.4}$). In table 3.4 the correlation length, ξ, is large after fully lithiation signifying increase in void size. With the help of Eq.3.6 radius of gyration, R_g, of the voids for carbon, $LiC_{10.4}$ and for LiC_5 can be calculated as 7.2Å, 7.0Å and 7.8Å , respectively.

From these scenario one point is clear that during partial lithiation almost all of the Li-ions intercalate in between graphene layers. This causes enlargement in d_{002} spacing between graphene layers. If lithiation is still continued, almost all of

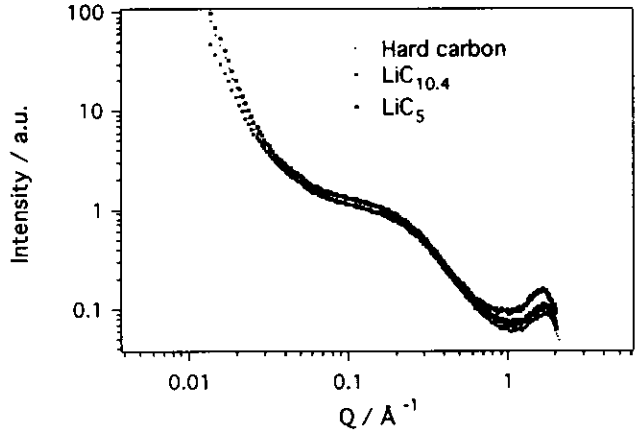

Figure 3.10:SANS data for hard carbon, partially lithiated hard carbon ($LiC_{10.4}$) and fully lithiated hard carbon (LiC_5).

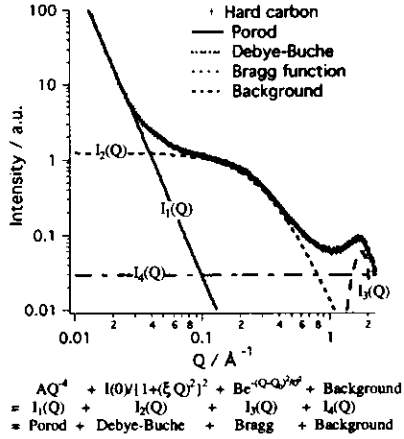

Figure 3.11: Components of fitting equation.

the extra lithiums go into the voids resulting in increase in void size and no further increase in d_{002} spacing takes place.

3.4.1 Low Temperature Experiments

Low Temperature Effect in NMR Experiments

From the work of K. Tatsumi [11] Fig. 3.17 shows ^{7}Li-NMR spectra of the fully lithiated non-graphitizable carbon fibers recorded at 25, -30, -70, and -150 °C. While the spectra of the fully lithiated non-graphitizable carbons gave one peak at 25 °C, the line shift of the peaks displayed a large variation, i.e., 13, 90, and 111 ppm (vs. LiCl) for the carbons heat-treated at 700, 1000, and 1200 °C, respectively.

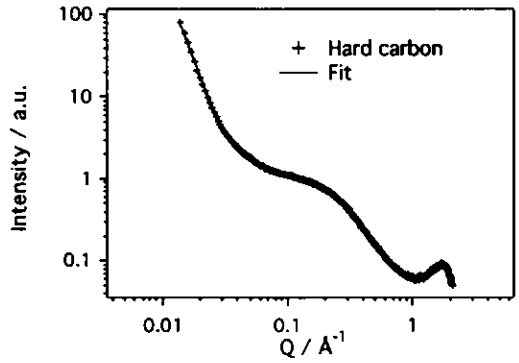

Figure 3.12: SANS data and fitting curves of hard carbon.

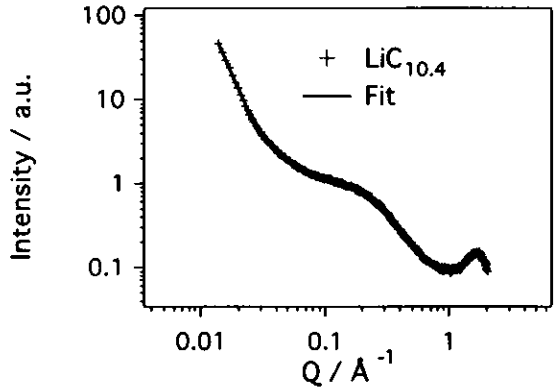

Figure 3.13:SANS data and fitting curves of partially lithiated hard carbon ($LiC_{10.4}$).

LiCl was used as the reference because Li is in fully ionic state in this compound. Carbon fiber (HTT 1200 °C) is our sample which we have studied by SANS. Since the ^{7}Li-NMR shift of lithium electrochemically inserted into graphitizable carbons is in the range from 0 to 50 ppm [51], it indicates a new type of lithium species in the carbon fibers heat treated at 1000 and 1200 °C. Moreover, the evidence for the new lithium species in the carbon fibers heat-treated at 1000 and 1200 °C was more obvious in the NMR spectra at low temperatures below -30 °C. Fully lithiated carbon fibers heat-treated at 1000 and 1200 °C showed a separation of NMR peaks below -30 °C; one signal above 100 ppm (the high field) and the other signal at ca. 20 ppm (the low field).

Fig.3.18 shows spectra of carbon fiber (HTT 1200 °C) at seven different temperatures. It does not show any hysteresis between cooling and heating. The line position (high field) shifts towards high ppm value and the line area (high field) decreases at low temperatures while line area (low field) increases. Moreover all the signals were deconvoluted to Lorentzian line shapes with line shift δ=18 (lowest field), 192 (middle field) and 281 (highest field) ppm (Fig. 3.19) [52]. These

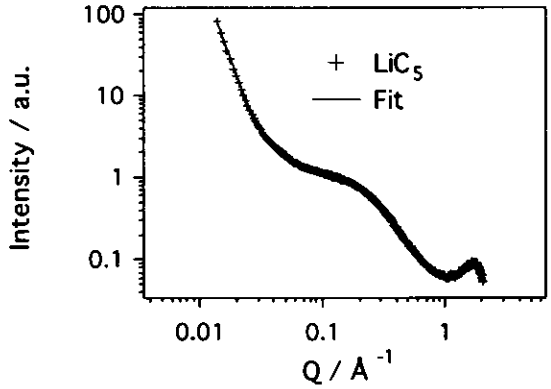

Figure 3.14: SANS data and fitting curves of fully lithiated hard carbon (LiC_5).

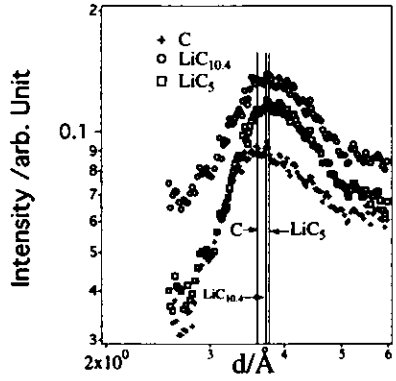

Figure 3.15: Enlarged version of Fig.3.10 in the Bragg peak region. Increase in d spacing in partially lithiated hard carbon signifies lithium intercalation in between graphene layers. C, $LiC_{10.4}$, and LiC_5 in the legend represent hard carbon, partially lithiated hard carbon, and fully lithiated hard carbon, respectively.

results thus indicate that the variation observed in the spectra is probably due to exchange of lithium nuclei among lithium species at different sites, and that the rate of exchange or thermal motion of lithium species slowed down on NMR time scale observed at low temperature, in agreement with the line broadening. No crystalline phase change occured during cooling and this was confirmed by SANS at low temperature which is discussed in the following subsection.

In general, ^{7}Li-NMR shift is independent of temperature for lithium species inbetween graphene layers as well as lithium metal. The peak position of the lowest field (δ=18 ppm) in Fig.3.18 is almost temperature independent and this signal corresponds to the lithium species in graphene layers. On the other hand, the other signals (middle and highest field) are quite novel because NMR shifts of the two signals increased with lowering temperature below 243 K as shown in

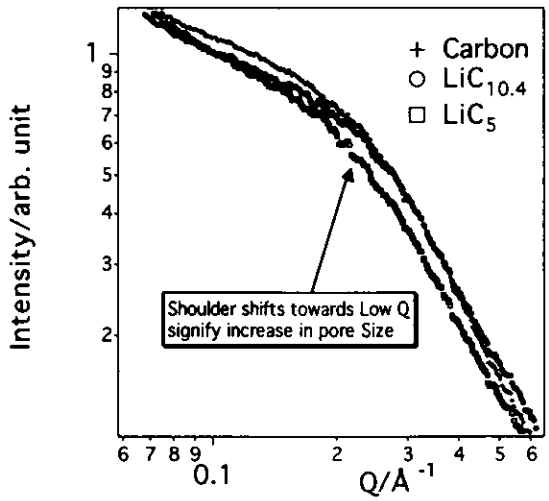

Figure 3.16: Enlarged version of Fig.3.10 in the shoulder region. Shoulder shift towards left in fully lithiated hard carbon (LiC_5) signifies increase in pore size which indicates lithium goes into pores.

Table 3.4: Fitting results: best-fit values obtained by Eq.(4.1) for the scattering curves of hard carbon, $LiC_{10.4}$, and LiC_5.

Sample Name	$I(0)$ (arb.unit)	ξ (Å)	d_{002} (Å)
carbon	1.24	2.94	3.72
$LiC_{10.4}$	1.10	2.85	3.80
LiC_5	1.12	3.19	3.87

Fig.3.20. Furthermore, the shift of the signal in the highest field is higher than that of the lithium metal(δ=262 ppm) [53] at low temperatures below 163 K. These two high shift signals correspond to the lithium species with metallic character in the void sites. We therefore propose the followings:

- The highly shifted signals (δ=281 and 192) are ascribed to "pseudo-metallic lithium and correspond to low voltage plateau of the discharge curve (Fig. 3.26(c)). Therefore, instead of temperature-independent Knight shift (as for lithium metal at 262 ppm), the NMR line exhibits a paramagnetic nature and shifts further when temperature decreases, following the increase in susceptibility.

- The lowest shift signal (δ=18) also shifts slightly with temperature change. Hard carbon presents small organized zones that can contain intercalated lithiums. However, the size of the crystallites is such that a complete π electrons delocalization may not be achieved (we will learn about delocalization

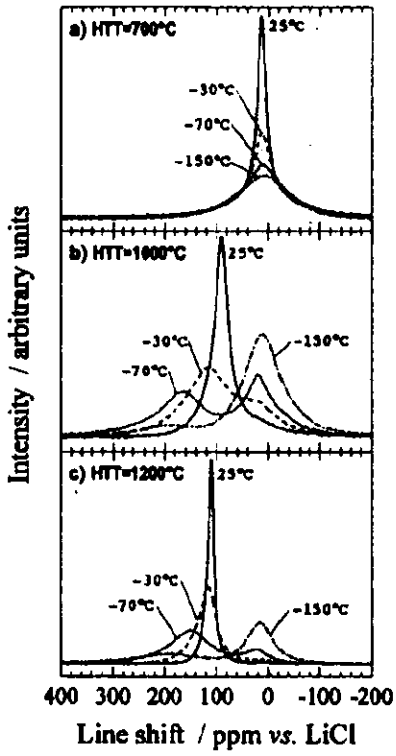

Figure 3.17: Variation of ^{7}Li-NMR spectra for the fully lithiated carbon fibers heat-treated at (a) 700, (b) 1000 and (c) 1200°C during cooling the samples; Reproduced from K. Tatsumi [11].

of carbon π orbital in a later section). Furthermore, the number of lithium ions intercalated in such a crystallite may not lead to LiC_6 composition obtained in pure graphite. Following these considerations, a paramagnetic-type behaviour is again expected for this signal.

Low Temperature SANS Experiments

As stated in the above subsection, ^{7}Li-NMR results suggested that the lithium species with metallic character forming clusters in the voids shows diffusive characteristic and to see if there is any effect on the pore structure, we performed SANS experiments on fully lithiated carbon fiber (HTT 1200 °C) at 300 K and low temperatures down to 96 K by SWAN. No significant change in scattering pattern was observed (Fig.3.21). These data were fitted by Eq.(3.2) using least squares and the fitting result is shown in Table 3.5. There is no change in the radius of gyration of pores and interlayer spacing, which indicates that the fully lithiated hard carbon structure does not change at low temperature and there is no net diffusion of lithium species from pore site to layer site and vice versa, rather they hopp from site to site and maintain a dynamic equilibrium in all possible sites.

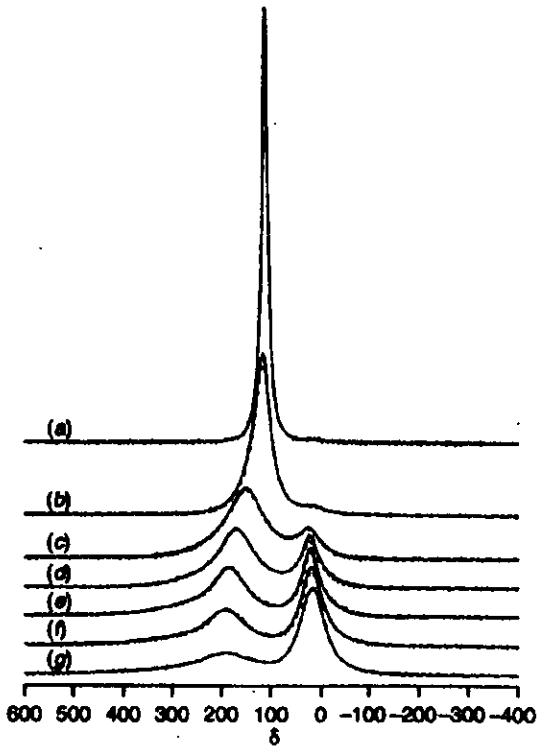

Figure 3.18: ^{7}Li-NMR spectra for the fully lithiated carbon fiber (HTT 1200°C) recorded at (a) 298, (b) 243, (c) 203, (d) 183, (e) 163, (f) 143 and (g) 123 K; solid line, at the direction of cooling; dashed line, heating; Reproduced from K. Tatsumi [52].

3.4.2 States of Lithium Species in Carbon Fiber

NMR is very sensitive to hyperfine interaction due to the partial presence of electron spins at the site of the probed nucleus. In the case of lithium in insertion compounds, such a presence is related to the degree of the presence of the charge transfer that occurs from lithium to the host, and to the possibility for electron spins formally present on atoms belonging to the host to posses a non-zero presence probability in the lithium 2s orbital. In the case of graphite, these electrons are located in the conduction band formed by the delocalized π orbitals of the carbon atoms forming the layer. The intercalation evidenced by ^{7}Li-NMR is therefore of a Knight shift type, due to Pauli paramagnetism of the electrons at the Fermi level, and thus depends on the participation of the 2s orbital of lithium in the conduction band.

One should also remember that what is characterized by NMR is mostly the electronic state of the lithium species very close to each other. For example, one can consider that the lithium species with a "covalent" bond with the carbon atoms are rather close to the "pseudo-metallic" ones that fill up the porosity. Therefore, the exchange between these two types of lithium as seen by NMR can occur with a simple rearrangement of the bonds, that is without significant movement of the

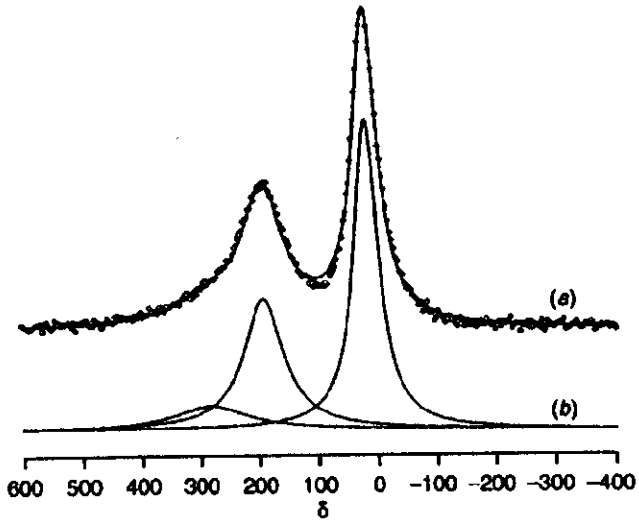

Figure 3.19: ^{7}Li-NMR spectra of fully lithiated carbon fiber (HTT 1200°C) at 143K: (a) experimental (o) and simulated (solid line) (b) deconvoluted spectra; Reproduced from K. Tatsumi [52].

lithium atom as such. This is particularly true within the porosity of the material. At low temperature, this electronic exchange is slowed down, and the different species are distinguished at the NMR time scale ($\sim 10^{-6}$ s).

A theoretical idea which has guided much of the research on graphite-intercalated compounds is that it is the π bands of each two-dimensional graphite layer which are being partially filled in the intercalation process [54]. The atomic configuration appropriate for graphite is $2s^1 2p_{xy}^2 2p_z^1$; the sp_{xy}^2 hybrids σ bonds, while the p_z states form the π bands. LiC_6 have a partial ionic character, Li having positive charge q and C having negative charge $\frac{1}{6}q$, corresponding to the atomic configuration Li $2s^{1-q}$ and C $2s^1 2p_{xy}^2 2p_z^{1+\frac{q}{6}}$, respectively. On the basis of band structure, it has been established that LiC_6 has occupied valence bands which are essentially those of graphite with an A-A layer stacking. This result indicates that LiC_6 is a π band metal and Li 2s states hybridize to some extent with low-lying graphite bands, particularly with a bonding π band contributing a covalent component to the interlayer bonding.

Fig. 3.22 illustrates electronic density map for the compound LiC_6, where it is clearly shown that there is an electron pocket at half the distance between Li and carbon atoms, which is suggestive of Li-C covalency. This map gives a good basis for electric field gradient (EFG) calculation on the nucleus core but can not fit the ^{7}Li NMR-Knight shift values.

G. Volpilhac, used a molecular calculation which does not give any band information but density of states and it needs some scaling. With only Li 2s orbital to hybridize with the carbon ones it gave too high values for the knight shift [55]. It was improved by Jebli [56]. He explicitely introduced the Li 2p orbitals. The admixture of the Li 2p contribution to the actual wave function is estimated as

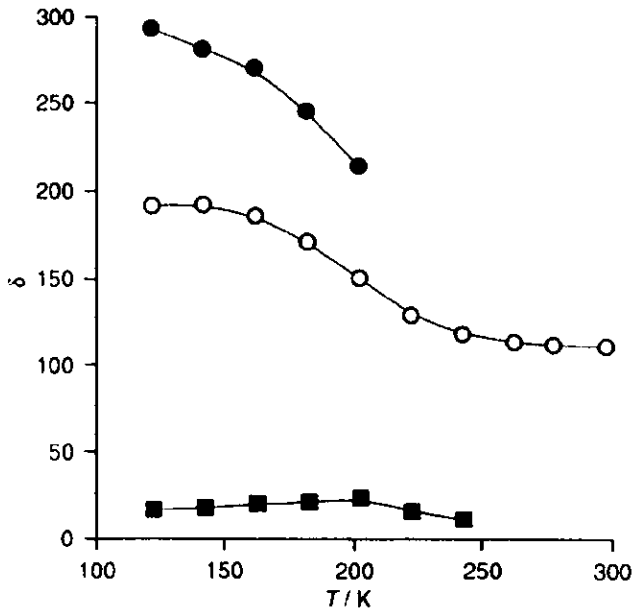

Figure 3.20: ^{7}Li-NMR shift of the signals determined by the curve fitting simulations as a function of temperature: the signals in the highest (•), the middle (o) and the lowest (■) fields in Fig. 3.19; Reproduced from K. Tatsumi [52].

30% of the whole Li-contribution. Then it fits the experimental Knight shift value very well.

As for the lithiums in void, there are two kinds of lithium: 1) lithiums that are not attached to the void surface are pseudometallic in the form of cluster, 2) a small amount of lithium which is attached to the void surface and encounter a different environment. Unlike intercalated lithium they interact with only one carbon plane and the band structure may be different. Here we might think of increased Li 2s orbital contributing to covalent bonding. This might be the reason why we observed Kinght shift (281 ppm) in one of the deconvoluted spectra (highest field), which is larger than that of metallic lithium (262 ppm).

So it can be concluded [57] that the occupied bands of LiC_6 are essentially those of graphite with A-A layer stacking. The conduction bands are formed from the π bands of graphite with an excess of $\frac{1}{6}$ electron/(C atom), making LiC_6 a π-band metal. An s-like band derived from the Li 2s state is completely unoccupied, lying at least 1.7 eV above the Fermi-level. The Li 2s state hybridizes to a small extent with a low-lying bonding π-band of graphite; but to negligible extent with the Fermi-level bands.

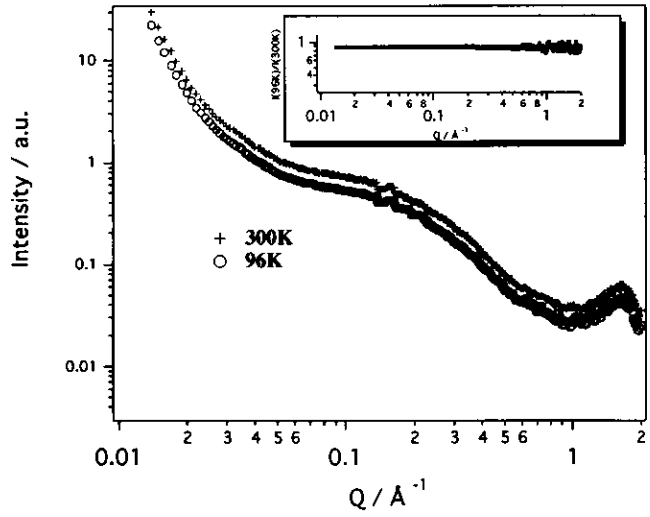

Figure 3.21:SANS data for fully lithiated carbon fiber (HTT 1200°C) at 300 and 96 K. 96 K data was offset for clarity. The inset shows the ratio between 96 K and 300 K data which is almost constant through the range indicating same structure.

Table 3.5: Fitting results: best-fit values obtained by Eq.(3.2) for the scattering curves of LiC_5 at 300 K and 96 K.

Sample Name	$I(0)$ (arb.unit)	R_g (Å)	d_{002} (Å)
LiC_5 (300K)	0.81	8.33	3.92
LiC_5 (96K)	0.70	3.30	3.93

3.5 Pore Density

3.5.1 Absolute Calibration of SANS data

Absolute calibration of scattering intensity was done for the calculation of number density and volume fraction of pores. This could be done by comparison with a standard of known cross section run in the same scattering geometry [58]. We used vanadium as the standard. It has large incoherent scattering cross section and Q independent scattering intensity. The calibration constant (scale factor in Fig.3.23) was calculated from the ratio of calculated intensity to observed intensity at high Q, where surface scattering could be avoided (Fig.3.23). This constant was used to plot absolute intensity in terms of differential cross section (cm^{-1}) vs. Q for hard carbon (Fig.3.24).

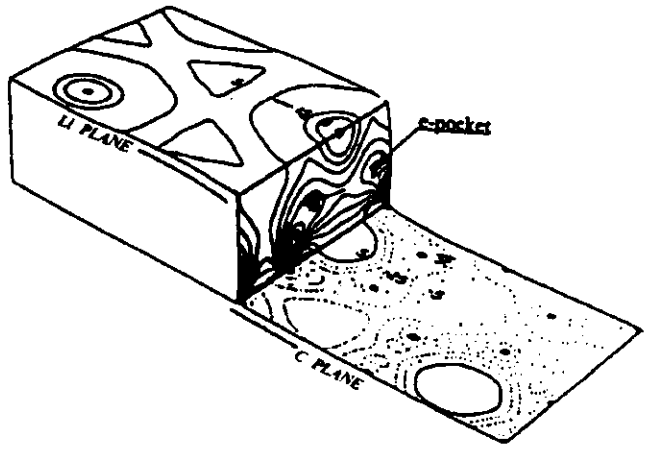

Figure 3.22: Contour plot of different electronic density due to LiC_6 formation. The presence of e-pockets at half the distance between Li and C atoms proves the partial Li-C covalency; Reproduced from J. Conard [55].

3.5.2 Calculation of Volume Fraction of Pores

Eq.3.3 could be used to calculate the number density of pores, n. previously $I(0)$ was obtained in arbitrary unit by fitting, which by multiplication with calibration constant, gave us absolute value of $I(0)$. $\Delta\rho$, the difference in scattering length density between carbon matrix and pore was calculated from density measurement according to JIS (Japanese Industrial Standard) K7112 which is described in the following section. V_P, the pore volume was calculated from the radius of gyration, R_g[4]. All these values of the variables in Eq.3.3 were used to calculate the number density of pores, n, as $4.77\times10^{19}/\text{cm}^3$, which multiplied with pore volume, V_P, gave us the volume fraction of pores as **16%**. These extra pore sites capable of intercalating lithium into hard carbon enabled us to intercalate up to a composition of LiC_5.

3.5.3 Density Measurement of Hard Carbon

Density measurement of carbon fiber was done using the method defined in JIS (Japanese Industrial Standard) K7112 and the following equation was used:

$$\frac{W_a - W_b + W_s}{D_{1-butanol}} = \frac{W_s}{D_s} \tag{3.7}$$

W_a = Weight of pycnometer and 1-butanol at a given volume (Fig.3.25),
W_b = Weight of pycnometer, 1-butanol and carbon fiber at the same volume,
W_s = Weight of carbon fiber,
D_s = Density of carbon fiber to be measured, and
D_s = Density of 1-butanol which was estimated by comparing weight of the same volume of pure water in a pycnometer (D_{water} at 23 °C = 0.9975 $g.cm^{-3}$).

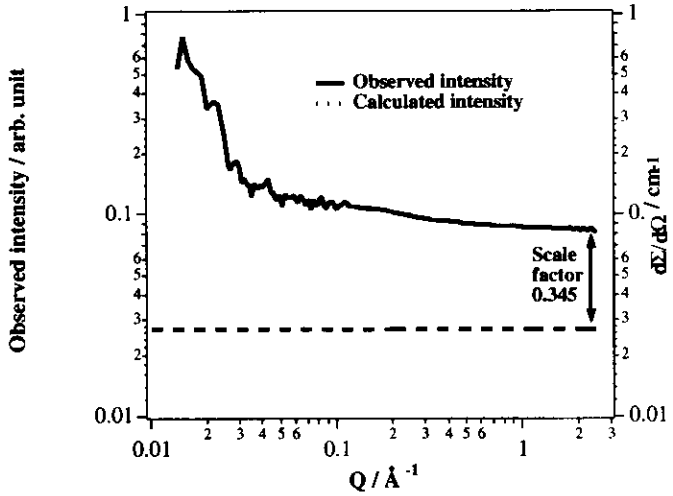

Figure 3.23:SANS data for vanadium. Left axis is scaled for observed intensity while right axis for calculated intensity interms of differential cross section per unit volume.

3.6 Irreversible Capacity and Hysteresis in Hard Carbon

From the studies on graphite, soft carbon and hard carbon we found hard carbon as the most promising material to be used for the anode of lithium-ion batteries. As shown in Fig.3.26 our petoca carbon fiber (hard carbon) sample with HTT 1200 °C shows considerably larger reversible capacity than other samples at different HTT's. This capacity exceeded the maximum theoretical capacity of graphite (372 mAh/g). But it also shows large irreversible capacity and hysteresis in voltage between charge and discharge. Now we need to eliminate these two problems. Some techniques are found in the literature to resolve these problems for other hard carbons as described below.

There are two mechanisms that contribute to the irreversible capacity in hard carbon: (1) reaction of lithium with electrolyte to form a passivation layer, (2) the reaction of lithium with surface functional groups or absorbed molecules that result from exposing the sample to air after pyrolysis. The electrolyte/lithium reaction will always occur to some extent unless electrolytes can be found that do not react with lithium. This reaction takes place on the surface of the electrode to form a passivation layer called the solid-electrolyte-interface (SEI). The surface area is more important than the surface chemistry and the formation of the SEI layer contributes about 50 mAh/g to the irreversible capacity. The second component is specific to hard carbon and contributes 150+ mAh/g [60].

Two processes have been found to lead to lower irreversible capacity in hard carbons prepared from sucrose [60]. The first is the chemical vapour deposition (CVD) of a carbonaceous substance from ethylene gas at temperatures > 700 °C and the second is lowering the dewatering temperature used to reduce the water

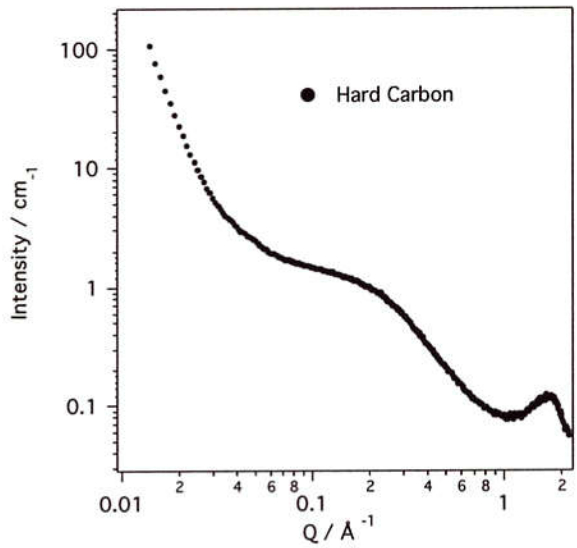

Figure 3.24: Absolute scattering intensity of SANS data for hard carbon.

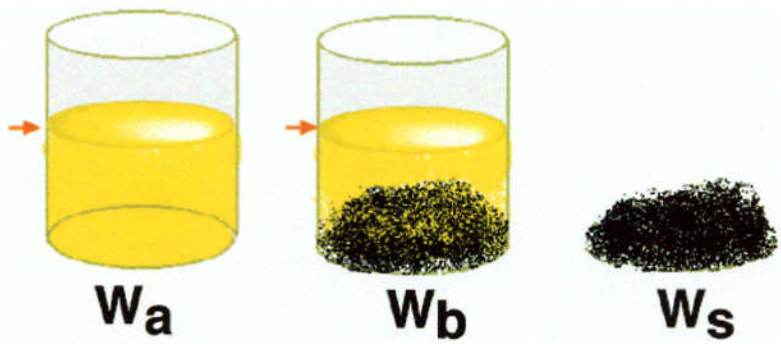

Figure 3.25: Density measurement of hard carbon by pycnometer and 1-butanol. Japanese Industrial Standard (JIS K7112).

content of the sucrose before pyrolysis. The former technique modifies the surface of the hard carbon before it is exposed to air and this produces a large reduction in the irreversible capacity from more than 150 mAh/g to less than 70 mAh/g (Fig.3.27).

The carbonaceous material deposited from ethylene is a soft carbon material with high hydrogen content. The voltage profile of this material is shown as the first curve in Fig.3.27. Such a material has a low commercial value however the low irreversible capacity is very significant.

The second method of lowering the irreversible capacity is to lowering the dewatering temperature. The dewatering process consists of heating raw sugar in an oven at temperatures between 150 to 180 °C. During this heating process the sugar will first melt, decompose and solidify. This pre-conditioning step drives off most of the water contained in the sugar. Then it is vacuum pyrolyzed. Fig.3.28

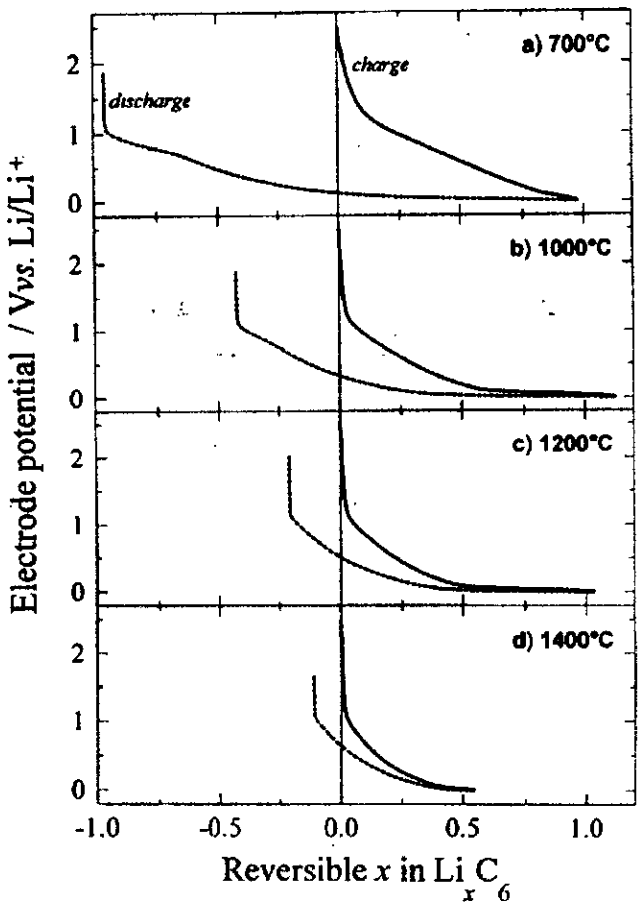

Figure 3.26: Galvanostatic discharge (dashed line) and charge (solid line) curves of the carbon fibers (different HTT) in 1 mol·dm^{-3} $LiClO_4$/EC+DEC (1:1 by volume) during the first cycle at a rate of 25 mA·g^{-1} [10].

shows the improvement in the irreversible capacity.

The large reversible capacity of hard carbon makes it a very attractive material to study with good potential for use in commercial batteries. The small hysteresis in the voltage profile degrades real battery performance and has been correlated to the residual hydrogen content after pyrolysis (<0.5% by mass) [59]. The hydrogen content, and hence hysteresis, can be reduced by heating the materials to higher temperatures during pyrolysis. However, there is a critical temperature above which the hard carbon begins to show a loss in reversible capacity (Fig.3.29).

The observed reversible capacity loss occurs primarily in the low voltage plateau component of reversible capacity and it is believed that the loss in reversible capacity is associated with the closure of nanopores at higher HTT [60].

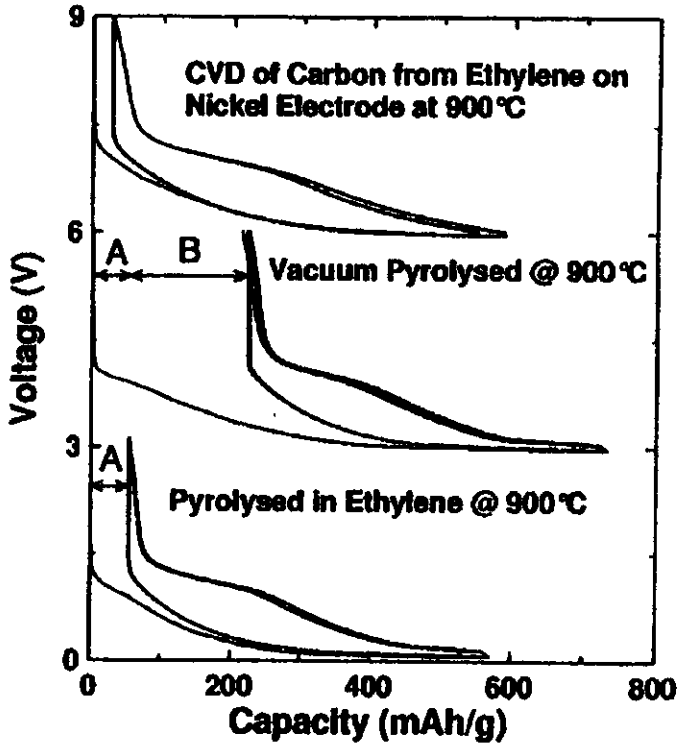

Figure 3.27:Voltage capacity profile for the specified samples. The data has been shifted sequentially by 3 V for clarity. The irreversible capacity in hard carbon is thought to contain two components; A: related to the formation of SEI layer and B: the component related to the reaction of lithium atoms with species absorbed from air in the nanopores of the sample [60].

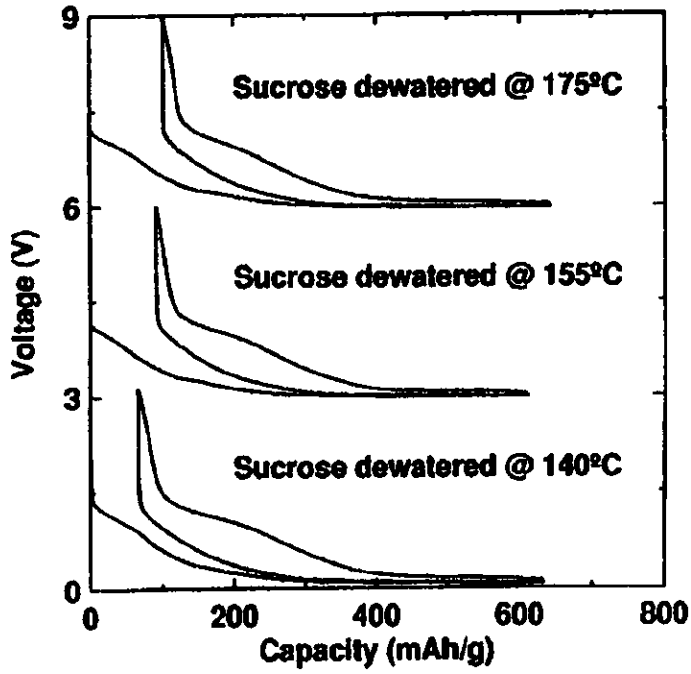

Figure 3.28: Voltage profiles of sucrose dewaterated to the specified temperatures followed by vacuum pyrolysis to 1050 °C [60].

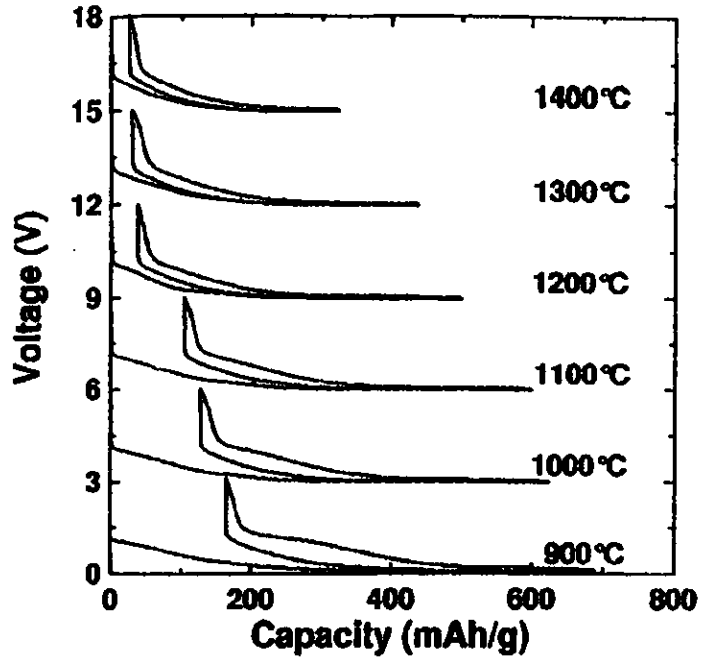

Figure 3.29: Voltage profiles of hard carbon prepared by pyrolysis of sucrose in argon gas. HTT's are indicated [60].

Chapter 4

Conclusion

In our study we tried to find out the structure of different functional carbon materials used as anodes of secondary (rechargeable) lithium-ion batteries. Effect of lithium intercalation on the structure of hard carbon was focused. From our study we can conclude the followings:

1. Small angle neutron scattering (SANS) measurement provided direct observation of nanopores and disordered structure in hard carbon. Lithium can be stored reversibly inside the pores by electrochemical intercalation resulting in higher reversible capacity ($\approx LiC_5$) which is substantially greater than the maximum theoretical capacity (LiC_6) of graphite.

2. During shallow lithiation process lithium first intercalates between the graphene layers of hard carbon which is concluded from the increase in *d*-spacing between the graphene layers, but no remarkable change in pore size was observed. Upon further deep charging *d*-spacing does not increase, but pore size increases indicating lithium intercalation into the pores.

3. Volume fraction of pores in hard carbon sample was measured $\approx$ 16%, which has a strong correlation with the capacity difference between our sample and pure graphite (LiC_6). We are much confident on this result because SANS technique is capable of probing every pore (open or closed, small or big) which is impossible by traditional gas adsorption techniques.

4. At low temperature ^{7}Li-NMR signal from metallic lithium disappeared indicating diffusion of lithium from pore sites. However, we did not observe any change concerning *d*-spacing and pore size in fully lithiated hard carbon at 96 K, suggesting no net diffusion of Li species from pore site to layer site and vice versa.

5. Unlike hard carbon we observed from the SANS measurement that MCMB and Swedish natural graphite (Woxna Fines) do not contain any pore structure. They offer lower reversible capacity (305 mAh/g for MCMB and from 340 to 371 mAh/g between crude and jet-milled Swedish natural graphite) compared to hard carbon.

6. Jet-milling of Woxna did not introduce any pore structure. However, from neutron powder diffraction (NPD) experiment we observed that the rhombohedral (ABC) phase content increased at the expense of hexagonal (AB) phase after jet-milling. This change in phase content increased the reversible capacity from 340 to 371 mAh/g.

Bibliography

[1] B. E. Warren, *J. Chem. Phys.*, **9**, 551 (1934).

[2] N. Takami, *Electrochim. Acta*, **42**, 2537 (1997).

[3] S. Yamada, H. Imoto, K. Sekai, M. Nagamine, *Electrochem. Soc. 191st meet. Ext. Abst.*, p.85 (1997).

[4] Y. Nishi, *Lithium Ion Batteries Fundamentals and Performance* (Ed. by M. Wakihara and O. Yamamoto), p.181, Kodansha and Wiley-VCH(1998).

[5] R. Yazami and M.Z.A. Munshi, *Handbook of Solid State Batteries and Capacitors*, p.425, World Scientific (1995).

[6] E. Peled *et al.*, *J. Electrochem. Soc.*, **143**, L4 (1996).

[7] K. Sato *et al.*, *Science*, **264**, 556 (1994).

[8] K. Suzuya, M. Furusaka, N. Watanabe, M. Osawa, K. Okamura, K. Shibata, T. Kamiyama, and K. Suzuki*J. Mater. Res.*, **11, No. 5**, 1169 (1996).

[9] T. Otomo, M. Furusaka, S. Satoh, S. Itoh, T. Adachi, S. Shimizu, M. Takeda, *J. Phys. Chem. solids*, **60**, 1579 (1999).

[10] K. Tatsumi *et al.*, *J. Power Sources*, **68** (1997) 263.

[11] K. Tatsumi, J. Conard, M. Nakahara, S. menu, P. Laugine, Y. Sawada, Z. Ogumi, *J. Power Sources* **81-82**, 397 (1999).

[12] Industrial Technology Research Institute, *ITRI Today*, **11**, From Web Page (1997).

[13] K. Ouchi and H. Honda, *Fuel*, **38**, 429 (1984).

[14] R. E. Franklin, *Proc. R. Soc. London Ser.*, A**209**, 196 (1951).

[15] B. E. Warren, *Phys. Rev.*, **59**, 693 (1941).

[16] T. Zheng *et al.*, *J. Electrochem. Soc.*, **142**, 2581 (1995).

[17] J. R. Dahn, T. Zheng, Y. Liu and J. S. Xue, *Science*, **270**, 590 (1995).

[18] A. Kozawa and K. V. Kordesch, *Progress in Batteries & Solar Cells*, **2**, JEC Press (1979).

[19] H. O. Pierson, *Handbook of Carbon, Graphite, Diamond and Fullerenes*, p.43, Noyes publications (1993).

[20] K. Inada, K. Ikeda, Y. Sato, A. Itsubo, M. Miyabashi and H. Yui, *Primary and Secondary Ambient Temperature Lithium Batteries* (Eds. by J. P. Gabano, Z. Takehara, and P. Bro), p.530, The Electrochemical Society (1988).

[21] O. Vohler, F. Von Sturm, E. Wege, H. Von Kienle, M. Voll and P. Klienschmitt, *Ullman's Encyclopedia of Industrial Chemistry* (Ed. by W. Gerhartz), 5th Ed., **Vol. 5A**, p.95, VCH (1986).

[22] A. Hérold, *Bull Soc. Chim. France*, **187**, 999 (1955).

[23] T. Tran and K. Kinoshita, *J. Electroanal. Chem.*, **386**, 221 (1995).

[24] D. Billaud, E. McRae and A. Hérold, *Mater. Res. Bull.*, **14**, 857 (1979).

[25] X. Y. Song, K. Kinoshita and T. D. Tran, *J. Electroanal. Chem.*, **143**, L120 (1996).

[26] Y. Nishi *et al.*, Richiumuion Nijidenchi no Hanashi, Shokabo (1997) (in Japanese).

[27] Y. Nishi, *Lithium Ion Batteries Fundamentals and Performance* (Ed. by M. Wakihara and O. Yamamoto), p.187-188, Kodansha and Wiley-VCH(1998).

[28] E. P. Barrett, L. G. Joyner and P. P. Halenda, *J. Am. Chem. Soc.*, **73(1)**, 373 (1951).

[29] D. Dollimore and G. R. Heal, *J. Appl. Chem.*, **14**, 109 (1964).

[30] G. Hovarth and K. J. Kawazoe, *Chem. Eng. Japan*, **16(6)**, 470 (1983).

[31] R. Evans, U. M. B. Marconi and P. Tarazona, *J. Chem. Soc. Faraday Trans II*, **82(10)**,1763 (1986).

[32] Z. Tan and K. E. Gubbins, *J. Phys. Chem.*, **94(15)**, 6061 (1990).

[33] P. J. Hall, S. Brown, J. Fernandez, J. M. Calo, *Carbon*, **38**, 1257 (2000).

[34] M. Furusaka *et al.*, *Proc. DANEF'97*, p. 14, in: S. Satoh*et al.*, *Proc. DANEF'97*, p. 86.

[35] T. Kamiyama *et al. Physica B*, **213-214**, 875 (1995).

[36] N. Watanabe *et al.*, *Jpn. J. Appl. Phys.*, **26**, 1164 (1987).

[37] J. D. Jorgensen *et al.*, *J. Appl. Cryst.*, **22**, 321 (1989).

[38] User Guide to Experimental Facilities at ISIS, RAL-92-041.

[39] R. K. Crawford *et al.*, *Proc. ICANS X*, Inst. of Phys. Conf. Ser. No. 97 (IOP Publishing, Newyork, 1989) P. 419.

[40] R. K. Crawford and J. R. Haumann, IEEE Trans. Nucl. Sci. NS-37 (1990) 72.

[41] M. Herstedt, H. Fransson, C. Bőrjesson, and K. Edström, Subm. to Electrochem. Soc. Proc. (2001)

[42] K. Edström, Dept. of Materials Chemistry, Ångström Laboratory, Uppsala University, Box 538 SE-751 21 Uppsala, Sweden, Private communication.

[43] T. Kasuh, A. Mabuchi, K. Tokumitsu and H. Fujimoto, *8th Int. Meet. Lithium Batteries*, Nagoya, Japan, Ext. Abst., p.97 (1996).

[44] H. Huang, E.M. Kelder, M.J.G. Jak, and J. Schoonman, *Solid State Ionics*, **139**, 67 (2001).

[45] C. Natarajan, H. Fujimoto, A. Mabuchi, K. Tokumitsu, and T. Kasuh, *J. Power Sources*, **92**, 187 (2001).

[46] J. R. Dahn and W. R. McKinnon, *J. Electrochem. Soc.*, **131**, 2823 (1984).

[47] J. R. Dahn, W. R. McKinnon, and S. T. Coleman, *Phys. Rev. B*, **31**, 484 (1985).

[48] T. Ohzuku *et al.*, *J. Electrochem. Soc.*, **140**, 2496 (1993).

[49] Agnès Claye and J.E. Fischer, *Electrochi.Acta*, **45**, 107 (1999).

[50] R. Kanno *et al.*, *J.PowerSources*, in press.

[51] K. Tatsumi *et al.*, *J. Electrochem. Soc.*, **143** (1996) 1923.

[52] K. Tatsumi *et al.*, *Chem. Commun.*, 687 (1997).

[53] G.C. Carter *et al.*, *Metallic Shifts in NMR, Part I*, Pergamon Oxford, 1977, p.239.

[54] N.A.W. Holzwarth *et al.*, *Phys. Rev. B*, **18**, 5190 (1978).

[55] J. Conard *et al.*, *TANSO*, **191**, 62 (2000).

[56] R. Jebli *et al.*, *J. Chim. Phys.*, **81**, 873 (1984).

[57] N.A.W. Holzwarth *et al.*, *Phys. Rev. B*, **18**, 5206 (1978).

[58] G. D. Wignal and F. S. Bates, *J. Appl. Cryst.*, **20**, 28 (1999).

[59] T. Zheng, W. R. McKinnon and J. R. Dahn, *J. Electrochem. Soc.*, **143 (7)**, 2137 (1996).

[60] E. Buiel and J. R. Dahn, *Electrochimia Acta*, **45**, 121 (1999).